Exploring dynamic phenomena due to sudden lifting of a thermal plate in a magnetized dusty medium

Sanatan Das[a,*], Soumitra Sarkar[b], Asgar Ali[c] and Rabindra Nath Jana[d]

[a] *Department of Mathematics, University of Gour Banga, Malda 732 103, India*

[b] *Department of Mathematics, Triveni Devi Bhalotia College, Paschim Bardhaman 713 347, India*

[c] *Department of Mathematics, Bajkul Milani Mahavidyalaya, Purba Medinipur 721 655, India*

[d] *Department of Applied Mathematics, Vidyasagar University, Midnapore 721 102, India*

Abstract

Magnetically influenced flow in conjunction with non-Newtonian dusty fluid finds wide-ranging applications in minerals processing, environmental engineering, and biomedical sciences. These include, but are not limited to, wastewater management, soil remediation and groundwater treatment, removal of contaminants from water or soil, magnetic separation, controlled and site-specific drug delivery, and biomedical diagnostics. The investigation pertains here to the dynamical behaviours of a conducting dusty fluid (Casson model) over a thermal plate with ramped motion, considering the influence of magnetic force. Other physical phenomena taken into account in the model include thermal emission, heat generation, and Newtonian heating wall conditions. Partial differential equations are used to impart the time-reliant flow mathematically. Analytic solutions are obtained through mathematical exercises employing the Laplace transform (LT). Graphs and tables are generated to illustrate changes in flow profiles and quantities caused by various physical factors. The research concludes that a higher thermal relaxation time parameter significantly improves thermal characteristics. The heat transfer rate and shearing stress on the plate exhibit temporal variations for a range of physical parameters. The particle concentration parameter has a notable impact on thermal transmission. The study's findings may be applied in climate modelling, weather prediction, contaminant transport, and studying phenomena such as dust storms, air pollution, and volcanic ash clouds.

Keywords: Dusty fluid; Casso model; magnetic field; Newtonian heating; thermal radiation; Laplace transform (LT)

1 Introduction

Dusty fluid (DF) refers to a heterogeneous mixture of liquid or gas containing suspended solid particles ranging in size from micrometres to nanometers. It is characterized by fine dust or particulate matter dispersed throughout the fluid medium. The behaviour and properties of dusty fluids are influenced by various factors, including the concentration, size, shape, and surface characteristics of the suspended particles, as well as the properties of the surrounding fluid. Dusty fluids exhibit unique flow behaviours, such as enhanced viscosity, non-Newtonian flow, or solid-like behaviour under specific conditions. They have wide-ranging applications in natural and industrial environments. For instance, atmospheric aerosols composed of dust particles suspended in air are prevalent in arid regions and areas with high pollution levels, impacting weather patterns, climate dynamics, and air quality. Dusty fluids find applications in diverse fields, including powder handling, cement production, soil remediation, groundwater treatment, transport of contaminants, drug delivery systems,

*Corresponding author e-mail: tutusanasd@yahoo.co.in

and pharmaceutical manufacturing. They are also relevant in geophysical studies, such as the investigation of sediment transport in rivers and coastal areas, as well as studying phenomena like dust storms, air pollution, volcanic ash clouds, and debris flows. The properties and behaviour of dusty fluids are the subjects of ongoing research and technological development. Several studies have explored various aspects of dusty fluid systems. Hamid et al. [1] conducted a thermal analysis of a fluid-dust suspension flowing on a stretching/shrinking surface, considering constant suction and dust particle slip. Mahanthesh et al. [2] unravelled the dynamics of an engine oil-based nano-liquid containing titanium oxide and dust particles on an accelerated isothermal plate and also discussed several other aspects, such as the results of nonlinear radiative heat, irregular heat source, and Hall currents. Nanjundappa et al. [3] theoretically assessed the ferro-thermal-convection phenomenon in a magnetized dust fluid within a Darcian porous layer. Radhika et al. [4] expounded the thermal behaviour of a dusty fluid containing suspended hybrid nanoparticles, considering uneven heat generation/absorption and magnetic field effects. For more detailed information on dusty fluids, refer to the works of Islam et al. [5] and Dey et al. [6].

The Casson fluid is a widely used non-Newtonian fluid model that effectively exposes the rheological characteristics of complex fluids such as suspensions, pastes, and biological fluids. It was first proposed by W.J. Casson, a British rheologist, in the mid-20th century [7]. Unlike Newtonian fluid models, which assume a linear dependance between shear stress and shear strain rate, the Casson model accounts for the nonlinear behaviour observed in these fluids. It introduces yield stress and a non-zero viscosity at zero shear rates, capturing the unique characteristics of non-Newtonian fluids. One significant advantage of the Casson model is its ability to accurately represent yield behaviour, which is commonly observed in many complex fluids. Yield stress is a crucial parameter that signifies the minimum stress required to initiate flow or deformation. The Casson model effectively describes phenomena such as flow initiation, wall slip, and flow behaviour in systems with a yield stress, making it applicable in diverse industries. The applications of the Casson fluid model span several fields. In the food industry, it is employed in processing various food products like sauces, dressings, and yogurts, optimizing their rheological properties for desired textures and consistencies. The oil and gas industry utilizes the Casson model to analyze the flow behaviour of drilling muds, optimizing their rheological properties for efficient drilling operations. In the pharmaceutical industry, it aids in understanding the viscosity and yield stress of pharmaceutical formulations. Additionally, the Casson fluid model finds applications in printing and inkjet technology, biomedical engineering, cosmetics and personal care products processing, paints and coatings, and more. However, it is worth noting that the Casson model is a simplification and may not capture the full complexity of real fluids accurately. It assumes constant yield stress and a square-root relationship between stress and strain rate, which may not hold in all scenarios. Nonetheless, the Casson fluid model provides a valuable framework for understanding and characterizing the flow behaviour of complex fluids, particularly those with yield stress, enabling process optimization and product development. Several research studies have further explored the applications of the Casson fluid model. Mahanthesh et al. [8, 9] addressed the thermal transmission in non-Newtonian fluid (Casson/Carreau model) dispersed with dust particles on an elongated surface accounting for the aspects of radiating thermal flux, exponential space-based heat source (ESHS), and convective condition. Hady et al. [10] delivered the numerical outcomes for the time-reliant convection in a dusty medium (Casson model)on a vertical wavy plate. Khan et al. [11] have investigated the fluctuating flow of a Casson two-phasic fluid containing tiny dust particles over inclined plate, considering the upshots of relative magnetic field and wall slip condition. Furthermore, several recent analyses on Casson fluids are provided in refs. [12–14].

Thermal radiation, the transfer of heat through electromagnetic waves such as infrared radiation, plays a significant role in non-Newtonian fluid flow. Various effects emerge when non-Newtonian fluids, which exhibit complex flow behaviour, interact with thermal radiation. The upshot of thermal emission on non-Newtonian fluid flow refers to the impact of radiative heat transfer on fluids

that do not adhere to Newton's law of viscosity. This interaction introduces additional factors affecting flow dynamics and heat transfer processes. In some instances, thermal radiation can induce changes in the flow behaviour of non-Newtonian fluids. For example, radiation-induced temperature gradients can alter the yield stress of yield stress fluids, leading to variations in flow initiation or cessation. It's worth noting that the repercussion of thermal radiation on the transport activity of non-Newtonian fluid depends on factors like fluid rheological properties, radiation intensity, optical characteristics, and flow configurations. Analyzing radiation-affected non-Newtonian fluid flow is challenging due to the complex interplay between these factors. Researchers employ numerical simulations, experimental techniques, and mathematical modelling to scrutiny the dominance of thermal emission on the streaming of non-Newtonian fluids. These approaches aid in understanding heat transfer mechanisms, predicting fluid behaviour, and optimizing system performance in practical applications, including polymer processing, food processing, and biomedical engineering. The study of radiating thermal flux in optically thin non-grey gases, which involves the interaction of thermal radiation with gases having non-uniform emissivity and low optical thickness is particularly significant. Understanding the behaviour of radiation in such gases is crucial for predicting heat transfer rates, optimizing energy systems, and interpreting remote sensing data. Consequently, the study of radiating thermal flux in optically thin non-grey gases finds applications in diverse fields, such as combustion, atmospheric science, and astrophysics. Several research studies have looked into the radiative aspects of non-Newtonian fluid flow. Cogley et al. [15] looked into the convection phenomenon in an optically thin non-grey gas. The consequences of magnetic force, Darcy resistance, Soret-Dufour, radiating thermal flux, and chemical reaction connected to the flow and energy fields of a conducting dusty fluid on a slopped plate that is being moved were unveiled by Pandya et al. [16]. Ghadikolaei et al. [17] numerically explained how the radiating heat flux affects the heat transmission in a non-Newtonian micropolar dusty nanofluid containing CNTs (carbon nanotubes) influenced by MHD and Joule heating effects over a plate that is being stretched. When exploring the dynamics of a dusty nano-liquid flow towards an upright plate, Mahanthesh et al. [18] looked into quadratic thermal convection and thermal radiation aspects. Krishna [19] has deliberated the radiative aspects of the MHD revolving stream of a Jeffrey fluid on a steep ramped/isothermal surface with perforations. Some other studies concerning thermal aspects can be found in refs. [20–22].

Newtonian heating refers to the phenomenon where a fluid in contact with a solid surface experiences heating, and the thermal distribution within the fluid is influenced by heat generation within the solid. This occurrence is commonly observed when there is significant heat dissipation within a solid object. A convective boundary condition is typically employed when studying thermal transmission between a solid surface and a fluid. This condition takes into account the convective heat transfer that transpires between the solid surface and the fluid. The convective boundary condition is based on Newton's law of cooling, which says that the thermal transmission rate between a solid surface and a fluid is proportional to the temperature difference between them. In the case of Newtonian heating, the convective boundary condition is modified to incorporate the temperature distribution within the solid. By applying the convective boundary condition with Newtonian heating, it becomes possible to analyze thermal transfer at solid-fluid interfaces where heat generation within the solid influences the thermal distribution in the fluid. Newtonian heating finds widespread use in various engineering applications, including heat exchangers, conjugate heat transfer around fins, cooling of electronic devices, and thermal management systems [23]. For instance, Das et al. [24] identified the upshot of Newtonian heating conditions on the thermal transport of a viscous fluid on a steep plate. The impact of magnetic force and Newtonian heating conditions on the flow patterns describing the transport of a Casson fluid on a flat plate was explained by Das et al. [25]. Upadhya et al. [26] conducted an inquiry into the magnetically influenced flow of dusty nanofluid (water-silver, water-gramene) across a stretched cylinder, considering the modified Fourier heat flux. Khan et al. [27] deliberated the radiative aspects of the magnetized Casson nanofluid flow on a thermal surface with Newtonian heating. Ali et al. [28], using an integral method, have reported on the upshot of

Newtonian heating on the revolving stream of a magnetized ternary hybrid nanofluid (Casson model) near a steep plate that is being moved with ramped velocity. Some important inquiries regarding convective boundary conditions are also covered in refs. [29–32].

When a magnetic field is introduced to a dusty fluid, it interacts with the particles, changing the flow dynamics and particle distribution within the fluid. The magnetic field exerts forces on the suspended particles, impacting their motion and distribution. The behaviour of the particles, such as alignment, aggregation, or dispersion, is influenced by properties like size, charge, and magnetic susceptibility, under a magnetic field. These behaviours, in turn, affect the fluid's overall flow patterns and particle concentration. In some cases, applying a magnetic field can induce modifications in the rheological traits of the dusty fluid. The magnetic forces can alter the apparent viscosity, shear-thinning behaviour, or fluid yield stress due to particle interactions or alignment. In summary, the introduction of a magnetic field has significant implications for dusty fluid flow, including influencing particle behaviour, altering flow profiles and affecting the rheological nature of the fluid. The understanding and utilization of these effects have far-reaching applications in areas such as mineral processing, environmental engineering, biomedical sciences, wastewater treatment, waste management, extraction and purification of valuable materials, removal of contaminants from water or soil, magnetic separation, controlled and site-specific drug delivery, and biomedical diagnostics. The ability to manipulate and control particle behaviour in fluids using magnetic fields presents opportunities for innovation and advancements across diverse industries, from medicine and biotechnology to materials science and environmental engineering. Researchers employ experimental techniques, computational simulations, and mathematical models to unfold the upshot of magnetic fields on fluid-dust phase stream. By considering the effects of magnetic field and thermal emission, Nandkeolyar et al. [33] analyzed the time-reliant flow caused by the sudden vertical movement of a ramped heating plate through a fluid-dust medium. Hazarika and Konch [34] scrutinized the magneto-convection phenomena in a dusty fluid near an upright plate with perforations to report the upshot of variable viscosity and thermal conductivity. Jalil et al. [35] delivered the analytical outcomes for the movement of a conducting fluid-dust suspension over a surface that is being stretched. Turkyilmazoglu [36] provided a mathematical approach to assess the transport phenomena in a fluid-dust suspension over perforated stretching/ shrinking surfaces with a quadratic surface temperature. The portrayal of heat transmission during water-based copper nano-liquid flow conveying tiny dust particles upon a stretched surface subject to a potent magnetic field was presented by Gireesha et al. [37]. It was proven that the dispersion of dust particles augments the Nusselt number. Abo-zaid et al. [38] have assessed the numerical results of the flow quantities associated with the flow-carrying nanoparticles and fine dust particles on a surface being stretched in the occurrence of heat flux. Examination revealed that the temperature drops with higher loading of dust particles. Hamid et al. [39] have spoken about the flow and thermal transmission in a ferrofluid that sustains dust particles on a perforated surface that is being moved. According to findings, the thermal transmission across the surface is reduced due to the dispersion of dust particles. Mishra et al. [40] have considered a conducting water-based nanofluid composed of copper and tiny dust particles to predict how the magnetic field would affect the fluid-particle suspension. It was resolved that the magnitude of shear stress for copper-water nanofluid is more minor than for silver-water nanofluid. Additional studies on magnetic dusty fluid flow can be found in refs. [41–43].

1.1 Objectivity and motivation

This study focuses on investigating the behaviour of a magnetized dusty (fluid-dust phase) over a thermal plate. Our motto here is to uncover the dynamics of a magnetized non-Newtonian fluid-dust phase (modelled using the Casson model) near an abruptly jumping plate, considering the upshots of heat origination and Newtonian heating wall condition. The model assumes the influence of radiation heat on the designed model, adopting the differential approximation [15] for thermal emission in an optically thin non-grey gas. Initially, the mathematical modelling study is conducted under

specific flow assumptions, followed by implementing the Laplace transform (LT) approach to generate analytical expressions of the flow variables. The study discusses and analyzes the physical upshots of various working factors within their respective ranges on the stream profiles and shearing stress, supported by relevant graphs. The numerical results of the thermal transmission rate are included in a table. A comparative elucidation is provided for the fluid-phase and dust-phase subjected to sudden lifting (SL) and uniform lifting (UL) of the plate. It is worth noting that this investigation has not been previously explored.

1.2 Novelty

To date, no investigation has been undertaken to unfold the dynamic phenomena arising from the ramped motion of a thermal plate in a magnetized fluid-dust medium. The current model introduces an innovative approach by examining the dynamics of a dusty fluid incorporating magnetic fields, thermal radiation, and ramped plate motion concerning the heat transfer process. These unique aspects distinguish our study and contribute to its novelty, that can be summarized as follows:

- This study is to explore the dynamic phenomena due to the ramped motion of a thermal plate in a magnetized fluid-dust medium.
- This study assimilates the Casson model to assess the rheological attributes of the non-Newtonian fluid-dust phase.
- The aspects of thermal emission, heat origination, and Newtonian heating boundary conditions are included in the flow model.
- The Laplace transform (LT) approach is implemented to generate analytical expressions of the flow variables.
- The results of this work led to the discovery of an exact solution for the ramped plate motion.

.

2 Modelling and solution

2.1 Physical illustration

Consider a 2D time-reliant laminar flow of an incompressible thermally radiative fluid-dust phase (dusty fluid) induced by a sudden lifting of a vertical thermal plate. The dusty stream is analyzed in the xy- plane; the x-axis is figured out along the vertical direction (i.e., flow direction), and the y-axis perpendicular to the flow direction. Fig.1 provides a conceptual representation of the flow configuration. Initially ($t = 0$), the thermal plate and surrounding fluid-dust suspension are at rest, maintaining a constant ambient temperature T_∞. As time progresses ($t > 0$), the plate located at $y = 0$ is lifted suddenly, with the plate velocity given by $u_0 t/t_0$ for $0 < t \leq t_0$, and a constant velocity of u_0 for $t > t_0$, where t_0 represents the characteristic time.. The magnetic field of constant intensity B_0 is replicated orthogonally to the plate. Additionally, the Newtonian heating condition is ascribed at the plate. The contribution of the induced magnetic field resulting from the fluid motion is neglected in this model. To account for the infinite extent of the thermal plate, the model variables are through to be dependent only on the spatial coordinate y and time t.

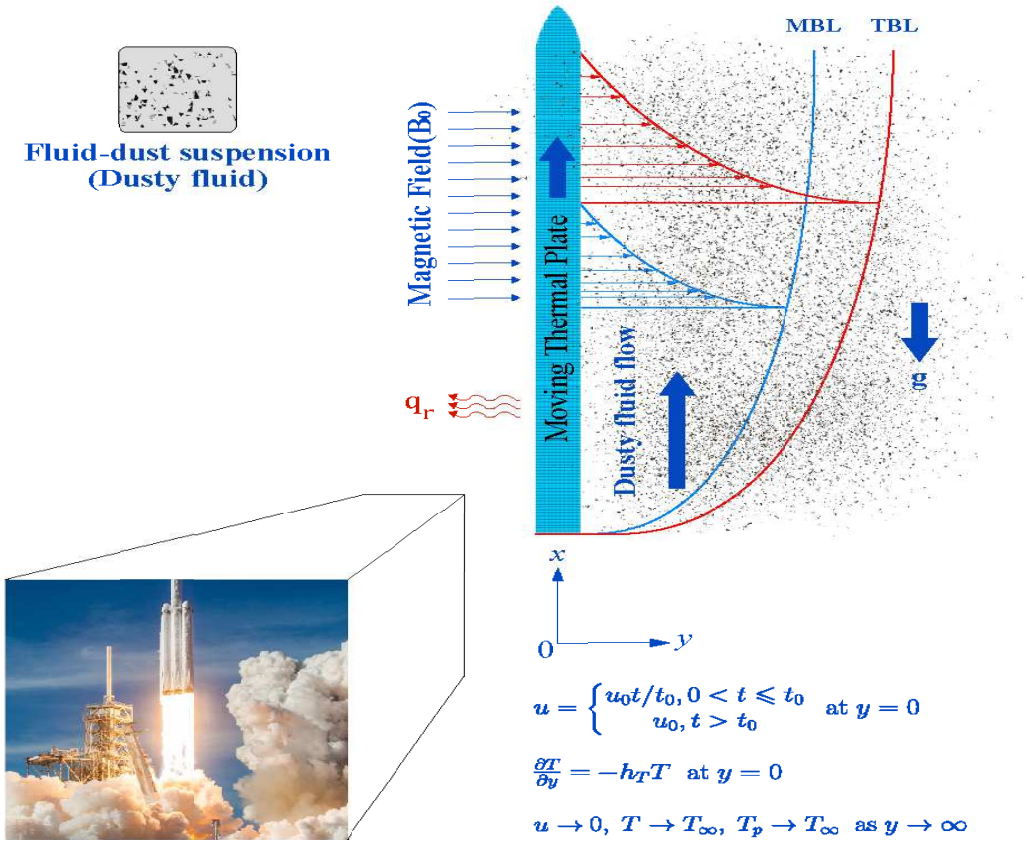

Fig.1: Conceptual representation of the flow configuration

2.2 Casson model

The stress tensor for an incompressible Casson fluid is defined as [11–14]:

$$\tau_{ij} = \begin{cases} 2(\mu_b + \frac{p_y}{\sqrt{2\pi}})e_{ij}, & \pi > \pi_c \\ 2(\mu_b + \frac{p_y}{\sqrt{2\pi}})e_{ij}, & \pi < \pi_c \end{cases} \tag{1}$$

where τ_{ij} refers to the stress tensor, e_{ij} the shear strain, μ_b the plastic dynamic viscosity, p_y the yield stress (the minimum stress required to initiate flow), $\pi = e_{ij}e_{ij}$, π_c the critical value of π based on the non-Newtonian model. For $\pi < \pi_c$, we reach

$$\tau_{ij} = \mu_b(1 + \frac{1}{\beta})2e_{ij}, \tag{2}$$

where $\beta = \frac{\mu_b}{p_y}\sqrt{2\pi_c}$ denotes the Casson parameter.

According to the Casson model, the fluid serves as a solid whilst the applied shear stress surpasses the yield stress. Once the yield stress is overcome, the fluid exhibits a square-root dependence of shear stress on the rate of shear strain. This unique square-root dependence is a distinctive characteristic of Casson fluids.

2.3 Flow controlling equations

The equations that form the fluid dynamics and thermal exchange of dusty fluid subject to the flow assumptions, and Boussinesq's approximations are written as follows [22, 28, 33]:

$$\frac{\partial u}{\partial t} = \nu(1+\frac{1}{\beta})\frac{\partial^2 u}{\partial y^2} - \frac{\sigma B_0^2}{\rho}u + \frac{k_0 N}{\rho}(v-u) + g\beta^*(T-T_\infty), \tag{3}$$

$$\frac{\partial u}{\partial t} = \frac{k_0}{m}(v-u), \tag{4}$$

$$\frac{\partial T}{\partial t} = \frac{k}{\rho c_p}\frac{\partial^2 T}{\partial y^2} - \frac{1}{\rho c_p}\frac{\partial q_r}{\partial y} + \frac{\rho_p c_s}{\rho c_p}(T-T_\infty), \tag{5}$$

$$\frac{\partial T_p}{\partial t} = \frac{1}{\gamma_T}(T-T_p), \tag{6}$$

where u refers to the fluid-phase velocity, v the dust-phase velocity, T the fluid-phase temperature, T_p the dust-phase temperature, ρ the fluid-phase density, ρ_p the dust-phase density, ν the kinematic viscosity, β^* the thermal expansion coefficient, c_p the fluid-phase specific heat at constant pressure, c_s the dust-phase specific heat at constant pressure, k the thermal conductivity of fluid-dust phase, σ the electrical conductivity of fluid-dust phase, g the acceleration due to gravity, N the number density of dust particles, m the average mass of a dust particle, k_0 the Stokes' resistance, γ_T the thermal relaxation time, t the time, and q_r the unidirectional radiative heat flux.

2.4 Thermal emission

Thermal emission in an optically thin non-grey gas refers to the phenomenon of heat transfer through radiation in a gas with a low optical thickness and exhibits non-uniform absorption and emission properties. In this context, *non-grey* implies that the gas does not have a constant or uniform emissivity across all wavelengths, and *optically thin* means that the gas is transparent to a significant portion of the incident radiation. The thermal emission/flux in an optically thin non-grey gas is portrayed mathematically as [15, 22, 28]:

$$\frac{\partial q_r}{\partial y} = 4(T-T_\infty)\int_0^\infty K_{\lambda_0}\left[\frac{\partial e_{\lambda_0}}{\partial T}\right]_0 d\lambda = 4(T-T_\infty)I, \tag{7}$$

where $I = \int_0^\infty K_{\lambda_0}\left[\frac{\partial e_{\lambda_0}}{\partial T}\right]_0 d\lambda$, K_{λ_0} is the radiation absorption coefficient, $e_{\lambda_0}(T)$ the Planck's constant, and the subscript 0 indicate that all the quantities associated with the thermal emission at T_∞.

When thermal radiation passes through an optically thin non-grey gas, several key characteristics come into play:

- Emissivity Variation: In an optically thin non-grey gas, the emissivity, which represents the efficiency of radiation emission, can vary with wavelength. This means that the gas absorbs and emits radiation differently at different wavelengths. As a result, the gas may selectively absorb or transmit certain wavelengths of radiation more than others, leading to variations in the thermal emission process.

- Spectral Radiative Flux: The radiative flux through radiation per unit area, is not constant across all wavelengths in an optically thin non-grey gas. Due to the varying emissivity, the spectral radiative flux differs at different wavelengths. This leads to variations in the intensity and distribution of radiative heat transmission within the gas.

- Radiative Heat Transfer Mechanisms: In an optically thin non-grey gas, radiative heat transfer occurs through several mechanisms, including emission, absorption, and scattering of radiation.

The gas may absorb radiation at specific wavelengths, emit radiation at different wavelengths, and scatter incident radiation in various directions. These mechanisms collectively contribute to the overall radiative heat transfer within the gas.

- Temperature Dependence: The radiative heat transmission in an optically thin non-grey gas is influenced by temperature gradients within the gas. Temperature variations affect the gas's emissivity, absorption, and emission characteristics, leading to changes in the radiative flux and heat transfer rates. This temperature dependence is important in determining the overall energy balance and temperature distribution within the gas.

On the substitution of(7), energy equation (5) turns into

$$\frac{\partial T}{\partial t} = \frac{k}{\rho c_p}\frac{\partial^2 T}{\partial y^2} - \frac{4}{\rho c_p} I(T - T_\infty) + \frac{\rho_p c_s}{\rho c_p}(T - T_\infty), \tag{8}$$

2.5 Wall conditions

The wall conditions for the model problem are [22, 28, 33]:

$$\begin{aligned} &t = 0 : u = v = 0,\ T = T_\infty,\ \ T_p = T_\infty \ \text{ for all } \ y \geq 0, \\ &t > 0 : u = \begin{cases} u_0 \frac{t}{t_0}, & 0 < t \leq t_0 \\ u_0, & t > t_0 \end{cases}, \frac{\partial T}{\partial y} = -h_T T \ \text{ at } \ y = 0, \\ &t > 0 : u \to 0,\ v \to 0,\ T \to T_\infty,\ \ T_p \to T_\infty \ \text{ at } \ y \to \infty, \end{aligned} \tag{9}$$

where h_T represents the convective heat transfer coefficient that represents the ability of the fluid to transfer heat by convection. It relies on factors such as fluid nature, flow configurations, and the geometry of the solid-fluid interface.

Time-dependent boundary conditions (TDBCs) capture unsteady flow phenomena' dynamic nature and characteristics. They allow for the modelling of transient events, ensuring a more realistic portrayal of flow behaviour during dynamic occurrences. In practical scenarios, boundary conditions such as velocities, temperatures, or concentrations often exhibit temporal variations. By incorporating TDBCs, the model can faithfully simulate and depict the evolving flow patterns and properties as they change over time. This becomes particularly crucial when investigating flow instabilities, flow start-ups, or the flow response to external perturbations.

2.6 Non-dimensional version

The following conversions are opted to get the non-dimension version of the model system [22,28,33]:

$$\eta = \frac{u_0 y}{\nu},\ \tau = \frac{u_0^2 t}{\nu},\ u_1 = \frac{u}{u_0},\ v_1 = \frac{v}{u_0},\ \theta = \frac{T - T_\infty}{T_\infty},\ \theta_p = \frac{T_p - T_\infty}{T_\infty}. \tag{10}$$

In view of (10), equations (3), (4), (8) and (6) in non-dimensional version are as follow:

$$\frac{\partial u_1}{\partial \tau} = (1 + \frac{1}{\beta})\frac{\partial^2 u_1}{\partial \eta^2} - M^2 u_1 + R(v_1 - u_1) + Gr\theta, \tag{11}$$

$$\frac{\partial v_1}{\partial \tau} = \frac{1}{\sigma_1}(u_1 - v_1), \tag{12}$$

$$Pr\frac{\partial \theta}{\partial \tau} = \frac{\partial^2 \theta}{\partial \eta^2} - Ra\,\theta + \frac{2}{3}R(\theta_p - \theta), \tag{13}$$

$$\frac{\partial \theta_p}{\partial \tau} = \gamma(\theta - \theta_p), \tag{14}$$

where $M^2 = \frac{\sigma B_0^2 \nu}{\rho u_0^2}$ signifies the magnetic parameter, $R = \frac{k_0 N \nu}{\rho u_0^2}$ the particle concentration parameter, $Gr = \frac{g\beta^* \nu T_\infty}{u_0^3}$ the Grashof number, $\sigma_1 = \frac{m u_0^2}{k_0 \nu}$ the particle relaxation time parameter, $Ra = \frac{4I\nu t_0}{\rho c_p u_0^2}$ the radiation parameter, $Pr = \frac{\rho \nu c_p}{k}$ the Prandtl number, $\gamma = \frac{\nu}{\gamma_T u_0^2}$ the temperature relaxation time parameter.

The non-dimensional version of the wall conditions are

$$\begin{aligned}
&\tau = 0 : u_1 = v_1 = 0,\ \theta = 0,\ \theta_p = 0 \ \text{ for all } \ \eta \geq 0,\\
&\tau > 0 : u_1 = \tau H(\tau) - (\tau - 1)H(\tau - 1) = \begin{cases} \tau, & 0 < \tau \leq 1 \\ 1, & \tau > 1 \end{cases}, \frac{\partial \theta}{\partial \tau} = -\alpha_0(1 + \theta) \ \text{ at } \ \eta = 0,\\
&\tau > 0 : u_1 \to 0,\ v_1 \to 0,\ \theta \to 0,\ \ \theta_p \to 0 \ \text{ at } \ \eta \to \infty,
\end{aligned} \tag{15}$$

where $\alpha_0 = \frac{h_T \nu}{u_0}$ refers to the Newtonian heating parameter, and $H(\tau)$ the Heaviside step function.

2.7 Laplace transform approach

The Laplace transform is a robust mathematical approach to solving partial/differential equations and analyzes dynamic systems. It offers several advantages over other solution techniques, such as direct integration or numerical methods. The Laplace transform exhibits linearity and superposition properties, allowing for the analysis of systems with multiple inputs or complex input signals. This property enables the analysis and design of systems with multiple components or inputs by considering the response to individual inputs separately and then superimposing the results. The Laplace transform has a convolution property that simplifies the analysis of linear time-invariant (LTI) systems. Convolution in the time domain corresponds to multiplication in the Laplace domain. This property enables the solution of partial/differential equations involving convolution integrals to be reduced to simple algebraic operations in the Laplace domain. The Laplace transform provides a convenient framework for the stability analysis of dynamic systems. These advantages make the Laplace transform a valuable technique for solving partial/differential equations and analyzing dynamic systems. Its ability to simplify complex problems, convert between time and frequency domains, and provide efficient solutions, making it widely used in various engineering and scientific disciplines.

Equations (11)-(14) with the wall conditions (15) are analytically resolved by implementing the LT approach. The LT corresponds to equations (11)-(14) are derived as:

$$\xi\, \bar{u}_1 = (1 + \frac{1}{\beta})\frac{d^2 \bar{u}_1}{d\eta^2} - M^2 \bar{u}_1 + R(\bar{v}_1 - \bar{u}_1) + Gr\, \bar{\theta}, \tag{16}$$

$$\xi\, \bar{v}_1 = \frac{1}{\sigma_1}(\bar{u}_1 - \bar{v}_1), \tag{17}$$

$$Pr\xi\, \bar{\theta} = \frac{d^2 \bar{\theta}}{d\eta^2} - Ra\, \bar{\theta} + \frac{2}{3}R(\bar{\theta}_p - \bar{\theta}), \tag{18}$$

$$\xi\, \bar{\theta}_p = \gamma(\bar{\theta} - \bar{\theta}_p), \tag{19}$$

The corresponding LT of the wall conditions (15) are:

$$\begin{aligned}
&\bar{u}_1 = \frac{1}{\xi^2}(1 - e^{-\xi}),\ \frac{d\bar{\theta}}{d\eta} = -\alpha_0(\frac{1}{\xi} + \bar{\theta}) \ \text{ at } \ \eta = 0,\\
&\bar{u}_1 \to 0,\ \bar{v}_1 \to 0,\ \bar{\theta} \to 0,\ \bar{\theta}_p \to 0 \ \text{ at } \ \eta \to \infty,
\end{aligned} \tag{20}$$

in which

$$\begin{aligned}
\bar{u}_1(\eta, \xi) &= \int_0^\infty u_1(\eta, \tau)\, e^{-\xi\tau}\, d\tau,\\
\bar{\theta}(\eta, \xi) &= \int_0^\infty \theta(\eta, \tau)\, e^{-\xi\tau}\, d\tau,
\end{aligned} \tag{21}$$

and $\xi(>0)$ represents the parameter related to LT.

Solutions of equations (16)-(19) under the conditions (20) are

$$\bar{\theta}(\eta,\xi) = -\frac{a_0}{\xi(a_0+\sqrt{\xi+b})}e^{-\eta\sqrt{a(\xi+b)}}, \tag{22}$$

$$\bar{\theta}_p(\eta,\xi) = \frac{\gamma}{\xi+\gamma}\bar{\theta}(\eta,\xi), \tag{23}$$

$$\begin{aligned}\bar{u_1}(\eta,\xi) &= \frac{1}{\xi^2}(1-e^{-\xi})e^{-\eta\sqrt{c(\xi+\lambda_1)}} - \frac{\lambda_3}{\xi(\xi-\beta_1)(a_0+\sqrt{\xi+b})}e^{-\eta\sqrt{c(\xi+\lambda_1)}} \\ &+ \frac{\lambda_3}{\xi(\xi-\beta_1)(a_0+\sqrt{\xi+b})}e^{-\eta\sqrt{a(\xi+b)}},\end{aligned} \tag{24}$$

where a_0, b, c, β_1, λ_1, λ_2, λ_3 are enlisted in appendix A.

The compact forms of $\theta(\eta,\tau)$, $\theta_p(\eta,\tau)$, $u_1(\eta,\tau)$, and $v_1(\eta,\tau)$ after taking the Laplace inversion of (22)-(24) are obtained as:

$$\theta(\eta,\tau) = \psi_1(\zeta_1,a_0,b,\tau), \tag{25}$$

$$\theta_p(\eta,\tau) = -\gamma a_0\psi_3(\zeta_1,a_0,b,-\gamma,\tau), \tag{26}$$

$$\begin{aligned}u_1(\eta,\tau) &= \psi_2(\zeta_2,\lambda_1,\tau) - H(\tau-1)\psi_2(\zeta_2,\lambda_1,\tau-1) \\ &+ \lambda_3[\psi_3(\zeta_1,a_0,b,\beta_1,\tau) - \psi_4(\zeta_2,a_0,\lambda_1,b,\beta_1,\beta_2,\tau)],\end{aligned} \tag{27}$$

$$\begin{aligned}v_1(\eta,\tau) &= \lambda_2[\psi_7(\zeta_2,\lambda_1,-\lambda_2,\tau) - H(\tau-1)\psi_7(\zeta_2,\lambda_1,-\lambda_2,\tau-1)] \\ &+ \frac{\lambda_2\lambda_3}{\lambda_2+\beta_1}[\{\psi_3(\zeta_1,a_0,b,\beta_1,\tau) - \psi_3(\zeta_1,a_0,b,-\lambda_2,\tau)\} \\ &- \{\psi_4(\zeta_2,a_0,\lambda_1,\beta_1,\beta_2,\tau) - \psi_4(\zeta_2,a_0,\lambda_1,-\lambda_2,\beta_2,\tau)\}],\end{aligned} \tag{28}$$

where $\zeta_1=\eta\sqrt{a}$, $\zeta_2=\eta\sqrt{c}$, and $\psi_i(i=1,2,...,7)$ are the dummy functions provided in appendix A.

For the sudden lifting (SL) of the plate, the non-dimensional version of the heat transfer rate $\theta'(0,\tau)$, and shearing stress τ^s are calculated from (25) and (27) and written as:

$$\theta'(0,\tau) = \frac{\partial\theta}{\partial\eta}\Big)_{\eta=0} = \sqrt{a}\,\psi_1'(0,a_0,b,\tau), \tag{29}$$

$$\begin{aligned}\tau^s &= \frac{\partial u_1}{\partial\eta}\Big)_{\eta=0} \\ &= \sqrt{c}\,[\psi_2'(0,\lambda_1,\tau) - H(\tau-1)\psi_2'(0,\lambda_1,\tau-1)] \\ &+ \lambda_3\sqrt{c}\,[\psi_3'(0,a_0,b,\beta_1,\tau) - \psi_4'(0,a_0,\lambda_1,\beta_1,\beta_2,\tau)],\end{aligned} \tag{30}$$

where $\psi_i'(i=,1,2,....,7)$ are derivatives of the dummy functions $\psi_i(i=1,2,...,7)$ and provided in appendix A.

2.8 Solution for uniform lifting

The closed-form expression for the flow field is computed subject to uniformly lifting (UL) of the plate [i.e. $u_1(0,\tau)$=1] as follows:

$$u_1(\eta,\tau) = \psi_8(\zeta_2,\lambda_1,\tau) + \lambda_3[\psi_3(\zeta_2,a_0,b,\beta_1,\tau) - \psi_4(\zeta_2,a_0,\lambda_1,\beta_1,\beta_2,\tau)] \tag{31}$$

For uniform lifting, and shear stress τ^u is evaluated as:

$$\begin{aligned}\tau^u &= \frac{\partial u_1}{\partial\eta}\Big)_{\eta=0} \\ &= \sqrt{c}\,\psi_8'(0,\lambda_1,\tau) + \lambda_3\sqrt{c}[\psi_3'(0,a_0,b,\beta_1,\tau) - \psi_4'(0,a_0,\lambda_1,\beta_1,\beta_2,\tau)].\end{aligned} \tag{32}$$

3 Validation of results

To validate our analytical approach, we compare the computed values of the velocity expression u_1 using the LT technique and the numerical technique, specifically the pdepe Solver in MATLAB R2021a, for the fluid-phase. The comparison is performed for fixed parameter values ($M^2 = 5$, $Gr = 5$, $\beta = 1$, $R = 2$, $\sigma_1 = 0.2$, $\tau = 0.5$) and the results are projected in Table 1. The closeness between the analytical and numerical data for u_1 confirms the accuracy of our analytical assessment, providing strong evidence of its reliability.

Furthermore, in a study by Nandkeolyar et al. [33] on the dynamics of a dusty fluid flowing upon a stationary vertical thermal plate, they searched the upshots of magnetic fields, thermal emission (using the Rosseland approximation), and a ramped heating condition on the flow. In our present research, we have developed a similar model considering the repercussion of a magnetic field, thermal emission (using the differential approximation), ramped plate motion, and the Newtonian heating condition on the flow. Remarkably, the findings of our investigation align well with those reported by Nandkeolyar et al. [33], reinforcing the consistency and validity of our study.

Table 1. Computed data for velocity expression u_1

	Analytical data	Numerical data (MatLab R2021a: pdepe Solver)
η	u_1	u_1
0.0	0.5010080000	0.500022500
0.5	0.1795570000	0.173542100
1.0	0.0606024000	0.061045000
1.5	0.0190847000	0.019010300
2.0	0.0055315600	0.005721320
2.5	0.0014554200	0.001555320
3.0	0.0003433070	0.000358950
3.5	0.0000718164	0.000077322
4.0	0.0000132027	0.000011000

4 Discussion of parametric behaviour

This section aims to assess and elucidate the repercussion of dissimilar working factors on the flow quantities. To demonstrate these variations, we present a series of graphical and tabular representations that showcase the analytic solutions and significant quantities derived from these solutions. These representations highlight the changes in dimensionless velocity, temperature, shearing stresses, and heat transfer rate across a range of characterizing parameters. Specifically, the magnetic parameter (M^2), Casson parameter (β), particle concentration parameter (R), particle relaxation time parameter (σ_1), radiation parameter (Ra), temperature relaxation time parameter (γ), Newtonian heating parameter (α_0), Prandtl number (Pr), and time (τ) are considered.

Figs.2-8 and Table 3 depict the variations in these distributions under different parameter values. The range/value of the working parameters utilized in this analysis is picked up from relevant literature and is listed in Table 2. A comparative deliberation is conducted for the fluid-phase, dust-phase, sudden lifting (SL), and uniform lifting (UL) of the plate. To generate graphs and tables, we employ the Mathematica. Overall, this examination encompasses four scenarios (fluid-phase, dust-phase, sudden lifting, and uniform lifting) and enables a comparative assessment of the dynamical behaviours of a magnetized fluid-dust suspension (dusty fluid).

Table 2. Ranges/values of working parameters /factors

Working parameters/factors	Range	Value	Source
M^2	$[0, 10]$	5	[33]
Gr	$[0, 10]$	5	[33]
β	$[0.5, \infty]$	1	[33]
R	$[0, 50]$	2	[33]
σ_1	$[0.2, 3]$	0.2	[33]
Ra	$[0, 50]$	2	[22, 28, 33]
γ	$[0.5, 3]$	3	[33]
α_0	$[0.5, 15]$	0.1	[28]
Pr	$[0.71, 7.1]$	7.1	[22, 33]
τ	$[0, 2]$	0.5	[22, 33]

4.1 Flow analysis

4.1.1 3D profile and streamlines

Figs.2(a-d) are here to canvas the 3D velocity profiles for the fluid-phase and dust-phase scenarios of the sudden lifting (SL) and uniform lifting (UL) of the thermal plate. These 3D plots showcase the variations in flow patterns as a function of space-time (η, τ) for four cases: fluid phase, dust phase, sudden lifting, and uniform lifting. In Fig.2(a), the velocity profile for the fluid-phase shows a gradual increase over time in the case of sudden lifting (SL), reaching a steady state condition. In contrast, for uniform lifting (UL), the velocity profile remains constant after the ramped nature is eliminated near $\tau = 1$. The 3D velocity profile under the uniform lifting condition is illustrated in Fig.2(b). Figs.3(a-b) illustrate the changes in streamlines patterns resulting from the sudden lifting and uniform lifting of the thermal plate. The streamlines associated with sudden lifting exhibit more pronounced curvature and are more orthogonal to the thermal plate compared to those associated with uniform lifting. These visual representations provide insights into the flow dynamics and the upshot of different plate motion scenarios on the fluid and dust phases.

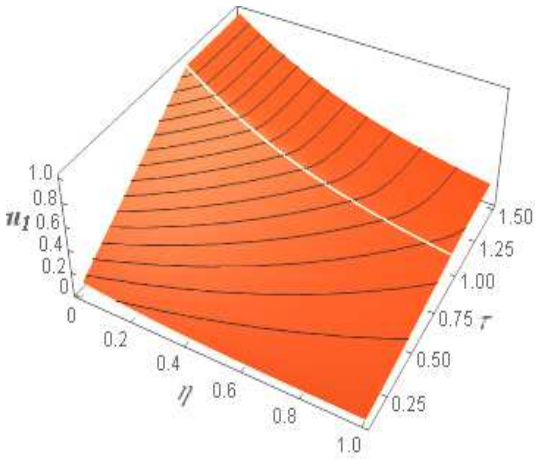

(a): Sudden lifting (SL)

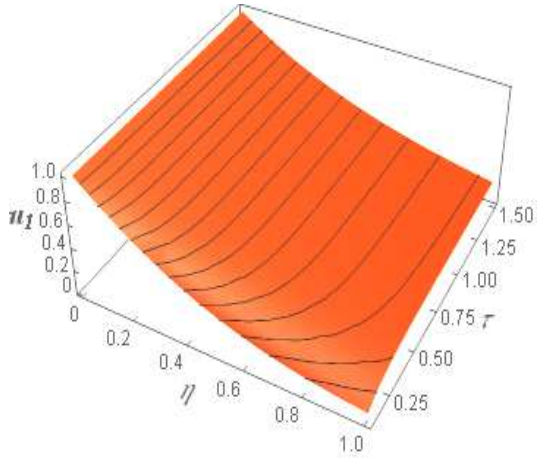

(b): Uniform lifting (UL)

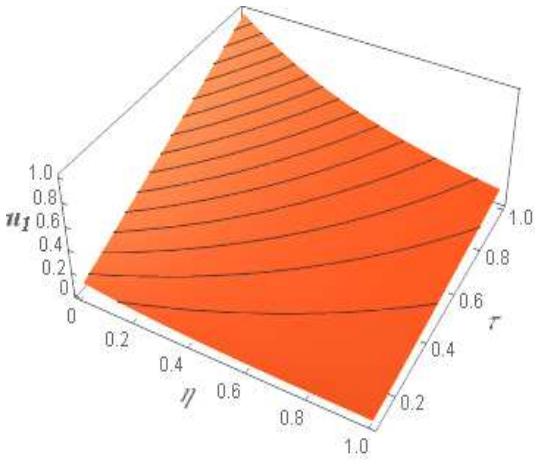

(c): Fluid-phase

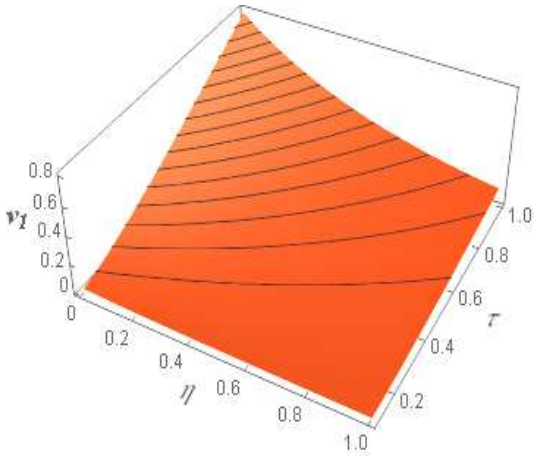

(d): Dust-phase

Fig.2: 3D velocity profile

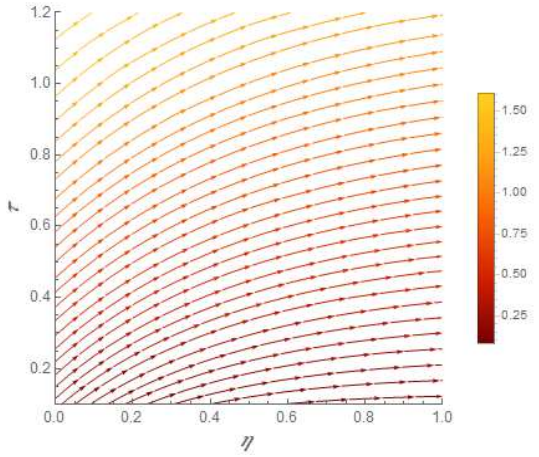

(a): Sudden lifting (SL)

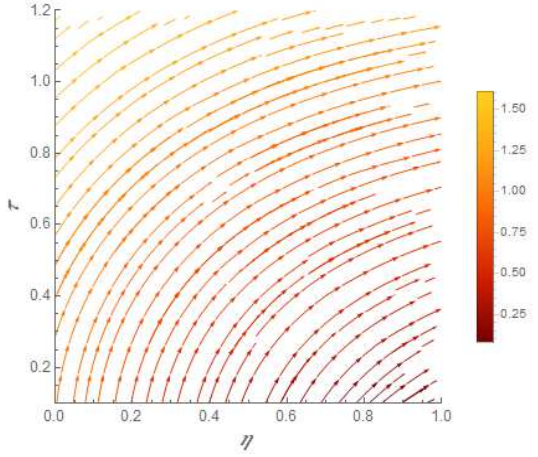

(b): Uniform lifting (UL)

Fig.3: Streamlines pattern

4.1.2 2D profile

For four different cases: fluid-phase, dust-phase, sudden lifting, and uniform lifting, the upshot of alters in magnetic parameter M^2 on the flow velocity u_1 is divulged in Figs.4(a-b). Mounting M^2 leads to significant damping of the flow velocity in both the fluid-phase and dust-phase, as shown in Fig.4(a). In Fig.4(b), the flow velocity curves for the sudden lifting and uniform lifting are seemed to be deteriorating by growing M^2. The increase in the levels of M^2 is associated with a strong Lorentz force, represented by the term $-M^2u_1$ in Eq.11. Because of this, the flow faces more resistance, causing a deceleration in the flow curve and reducing the thickness of the momentum zone. A value of $M^2 = 0$ indicates the non-occurrence of a magnetic field, while $M^2 > 0$ represents the effective repercussion of the magnetic field on flow dynamics. The outcomes reveal that the magnetic parameter significantly affects the flow momentum, which in turn affects the dusty fluid dynamics. Figs.4(c-d) interpret the upshot of Casson parameter β on the flow field. As seen in the figures, it is proven that augmented β contributes to less resistance to the fluid being flowed. This is related to the fact that a rise in Casson parameter weakens the yield stress, due to which the fluid motion impedes. To analyze how the particle concentration parameter R affects the flow velocity, we refer to the data shown in Figs.4(e-f). It is examined here that the higher levels of R correspond

to slower fluid flow. This phenomenon can be physically explained by the fact that larger values of R (represented by the term $R(v_1 - u_1)$ in Eq.11) increase the particle concentration, leading to emaciation in the velocity profile and the stiffness of the boundary layer.

The dispersion of the velocity profiles with respect to the particle relaxation time parameter σ_1 is shown graphically in Figs.4(g-h). The line graph clearly communicates that as values of σ_1 are increased, the velocity curve also increases. As σ_1 grows larger, the momentum diffusivity is appeared to boost. Due to this reason, the velocity curve experiences a moderate augmentation due to the particle relaxation time. Figs.4(i-j) showcase the characteristics of time-reliant flow for four cases: fluid-phase, dust-phase, sudden lifting, and uniform lifting. The results demonstrate a notable growth in the unsteady flow profile for all cases as time τ continues. These results provide valuable insights into the interaction between the time and the flow field, determining the time-dependent behaviour of the system under investigation. Figs.4(a-j) compare the flow velocity graphs. These graphs communicate that the flow velocity in the dust-phase is slower than that in the fluid-phase. This distinction arises from the relatively higher viscosity of the dust phase compared to the fluid phase. Furthermore, as depicted in Figs.4(a-j), the flow velocity is lower for sudden lifting and higher for uniform lifting.

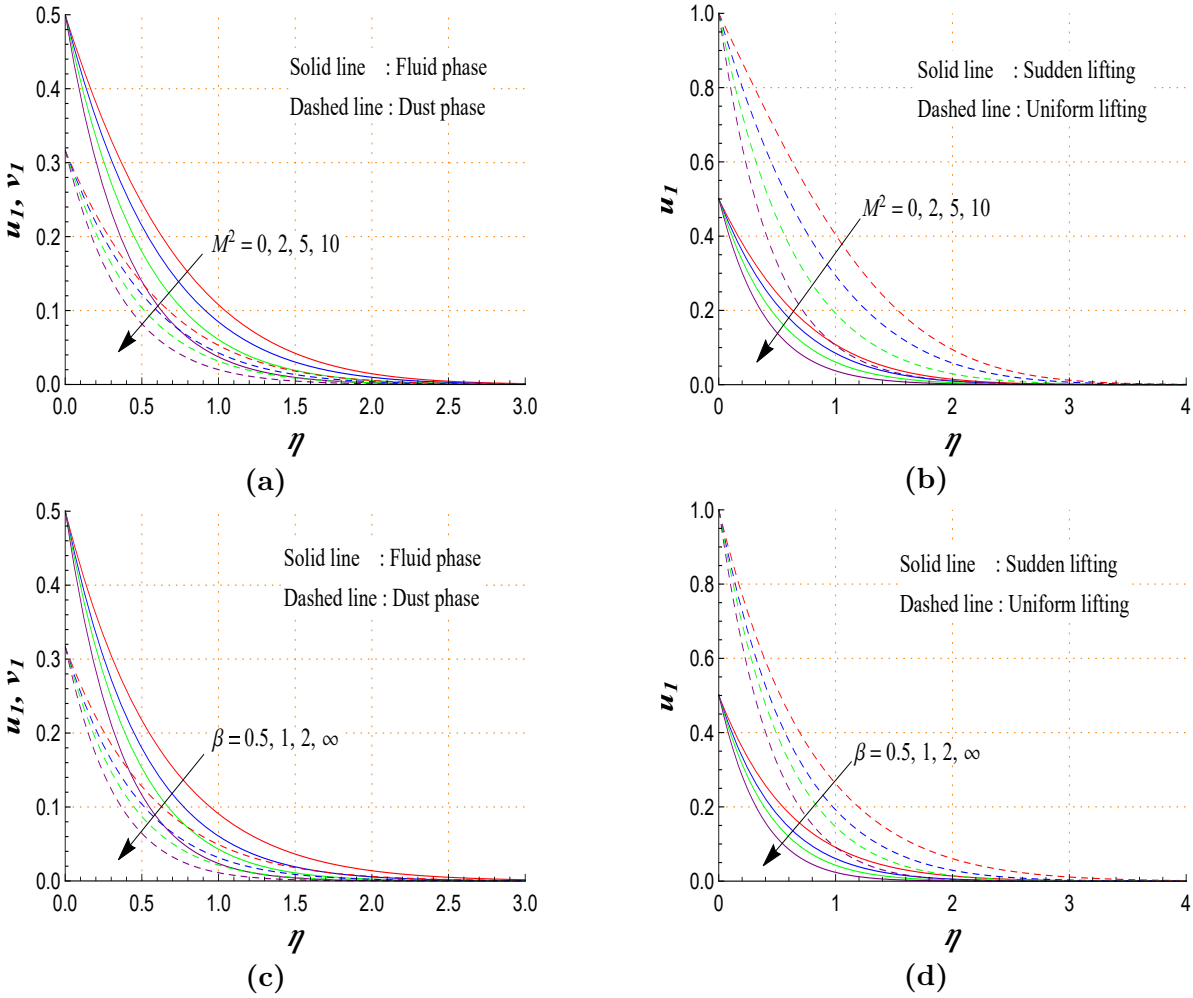

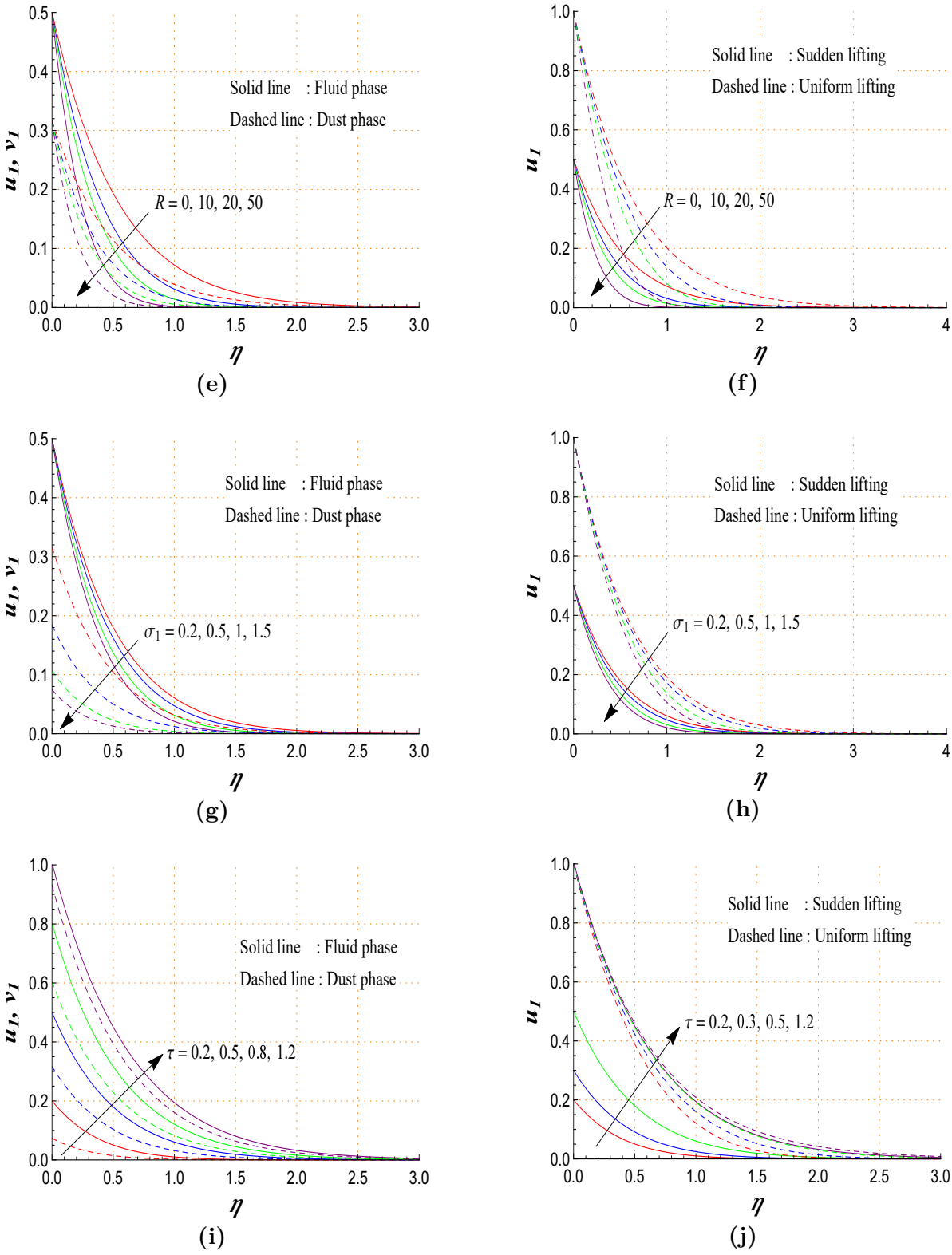

Fig.4: Dispersion of velocity distribution due to working factors

4.2 Thermal analysis

4.2.1 3D profile and heatlines

Figs.5(a-b) provide a 3D visual representation of the thermal field θ concerning the fluid-phase and dust-phase. These 3D plots are here to expose the modulation of temperature due to variation in unison of space-time (η, τ). The fluid-phase temperature is higher compared to the dust-phase. Examining the heatlines pattern in Figs.6(a-b), it can be observed that they exhibit minimal curvature.

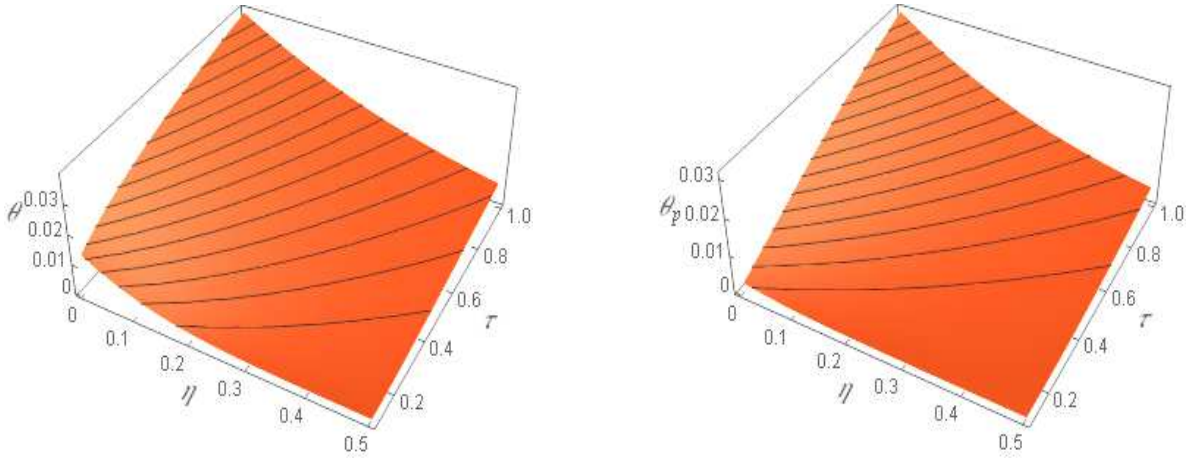

(a): Fluid-phase **(b)**: Dust-phase

Fig.5: 3D heat profile

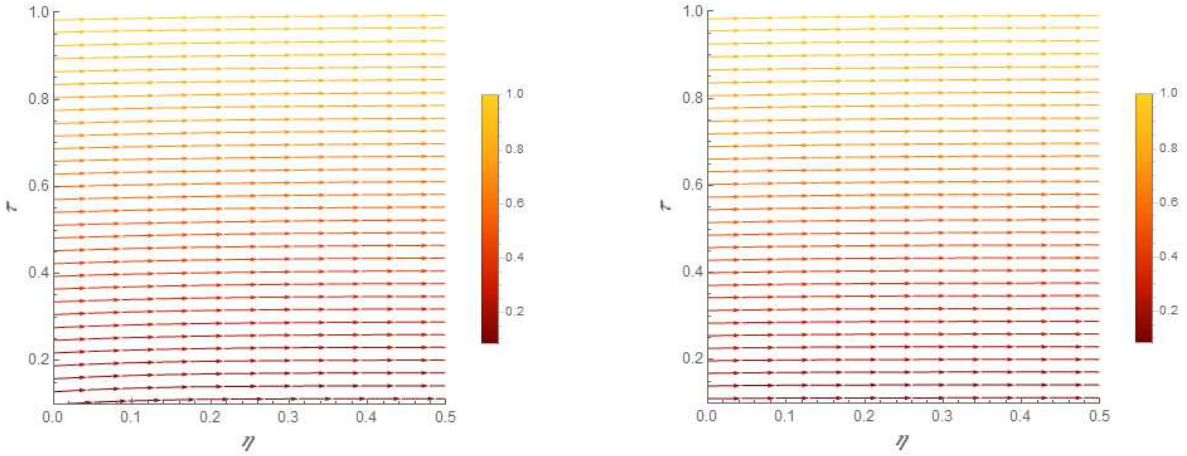

(a): Fluid-phase **(b)**: Dust-phase

Fig.6: Heatlines pattern

4.2.2 2D profile

Fig.7(a) communicates graphical illustrations of the thermal field with respect to variations in radiation parameter Ra for both the fluid-phase and dust- phase. As the value of Ra augments, the thermal profile exhibits a downturn for both cases. This behaviour is consistent with the findings of Das et al. [22], highlighting the impact of heat radiation on the thermal profile. The increased value of radiation parameter results in higher heat energy being emitted from the fluid region through thermal flux radiation. Consequently, more energy is transferred through the thermal plate surface, leading to the flow thermal level degeneration. These results enhance our understanding of the dynamics within the investigated flow system. The repercussion of particle concentration parameter

R on the thermal curve is investigated in Fig.7(b). The thermal curve declines as R swells, regardless of whether it is the fluid-phase or dust-phase. This figure provides valuable insights into the thermal distribution influenced by the concentration of dust particles in the analyzed flow system. Fig.7(c) elucidates the thermal distribution, taking the temperature relaxation time parameter γ into account. The graph demonstrates that the increased temperature relaxation time parameter has a boosting influence on the thermal profile. This suggests that the temperature relaxation time parameter regulates the thermal distribution within the flow system. The change in the temperature due to the Newtonian heating parameter α_0 is publicized in Fig.7(d). It is characterized that a notable uprising in the flow temperature is induced by rising α_0's value. As α_0 approaches infinity, the Newtonian heating condition approaches the prescribed wall temperature case. The graph reveals that higher values of α_0 correspond to higher temperatures in the flow region.

Fig.7(e) manifests the thermal distribution as a function of the increasing influence of the Prandtl number Pr. As the Prandtl number grows from $Pr = 0.71$ (air) to $Pr = 7.1$ (water), the thermal field diminishes for both the fluid-phase and dust- phase. This behaviour can be attributed to the fact that higher values of Pr reduce the strength of heating source terms in the energy equation, resulting in a decrease in flow temperature. Additionally, the graph reveals that increasing the Prandtl number shrinks the thermal zone's width. This admits that the Prandtl number plays a vital role in influencing the system's thermal performance, consequently leading to temperature variations within the system. From Fig.7(f), it is noticed that as time progresses, the temperature rises. This can be attributed to the faster heat flux in the dust-phase compared to the fluid-phase. Notably, the graph of the thermal field for the fluid-phase consistently exhibits higher values, while the dust-phase shows lower values. This suggests that the fluid-phase has a weaker heat conduction property compared to the dust-phase.

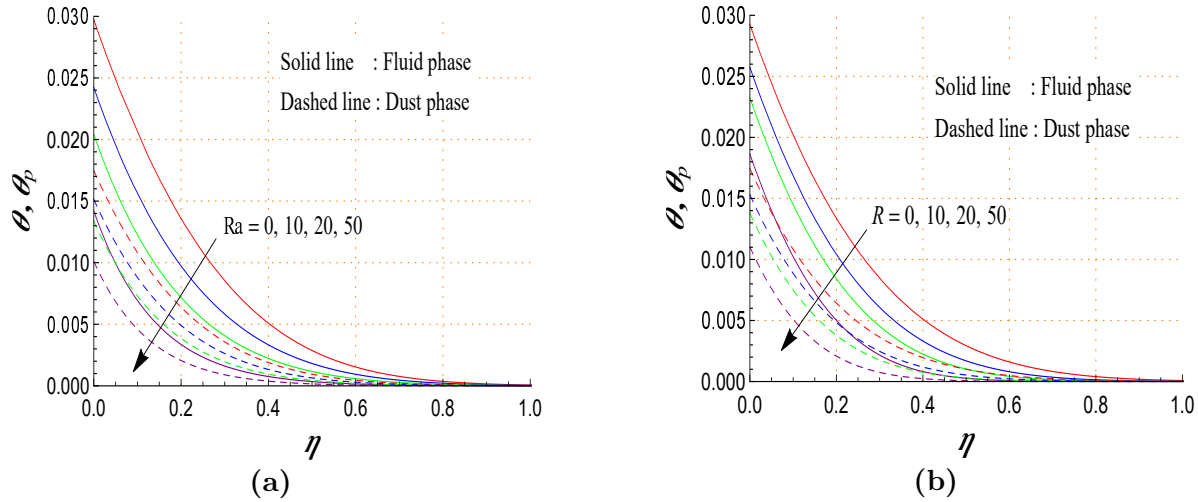

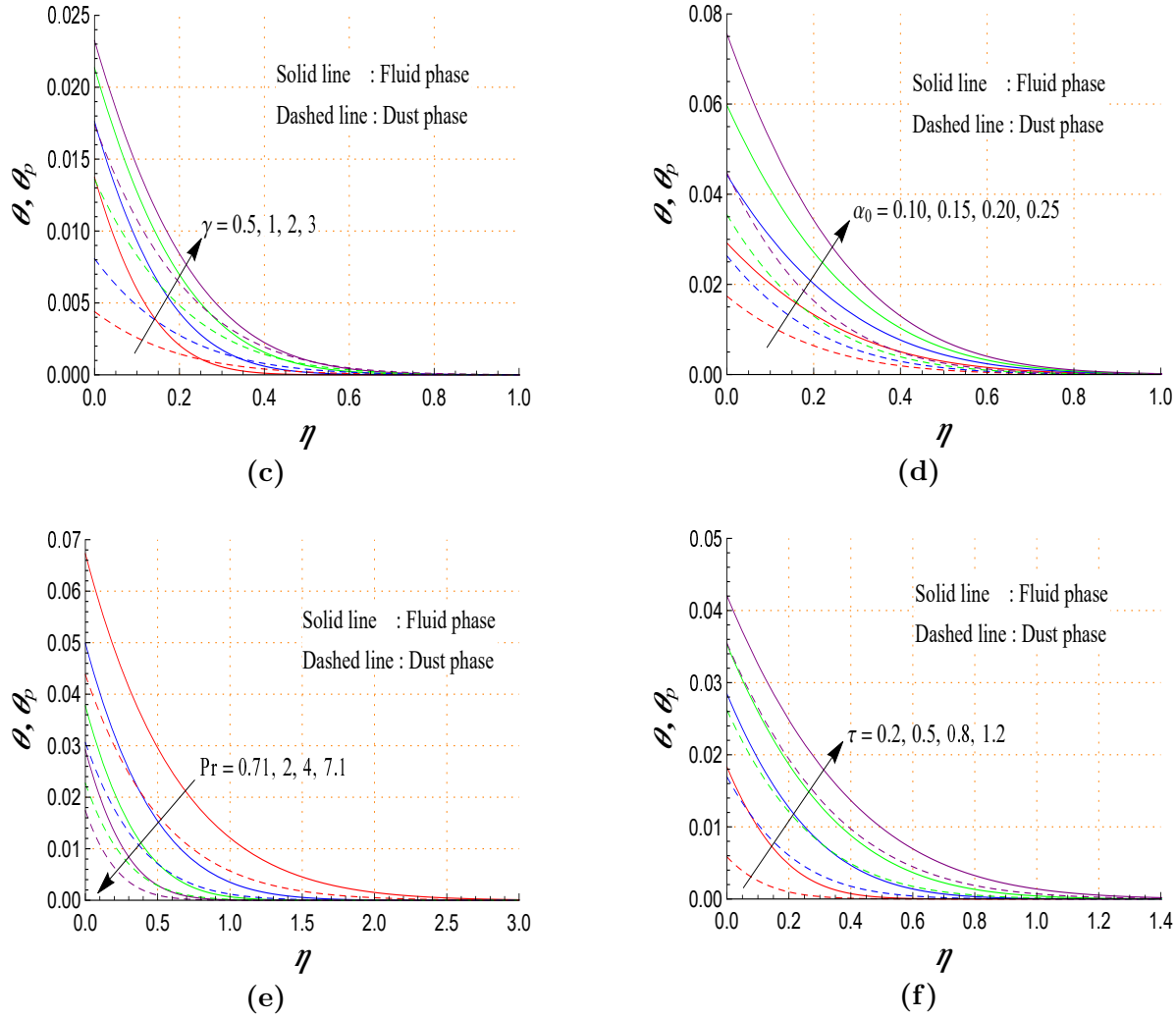

Fig.7: Dispersion of thermal distribution due to working factors

4.3 Shearing stress analysis

Figs.8(a-d) highlight the upshot of the model factors, namely (M^2, β, R, σ_1, τ) on the dimensionless shearing stresses (τ^s, τ^u) under the sudden lifting (SL) and uniform lifting (UL) conditions. Analyzing these graphs, it becomes evident that as the values of (M^2, β, R, σ_1) are increased, the absolute values of shearing stresses (τ^s, τ^u) also increase, except for the case of uniform lifting where they decrease with time τ. This observation indicates that higher values of (M^2, β, R, σ_1) result in a greater force exerted on the moving thermal plate, leading to increased shear tension. Specifically, an increment in the estimates of magnetic parameter M^2 leads to higher amounts of shearing stresses ($-\tau^s$, $-\tau^u$) due to a reduced fluid velocity in the boundary layer caused by the mastery of the Lorentz force. The Lorentz force slows down the fluid flow, resulting in a reducing in the depth of the boundary region and an amplification in the absolute values of shearing stress on the plate, as depicted in Fig.8(a). Examining the shearing stress profiles shown in Figs.8(b-d), it is seen that an increase in (β, R, σ_1) enfeebles the velocity gradient. As a consequence of the reduced momentum boundary layer, the wall shear stress increases, leading to shearing stress on the plate. Notably, there is a significant rise in shearing stress near the point $\tau = 1$ with increasing time τ only in the case of sudden lifting (SL) of the plate. This can be attributed to the exchange from a ramped to uniform speed at the point $\tau = 1$. The absolute value of shearing stress for the sudden lifting of the plate near τ is much higher compared to the uniform lifting of the plate. These figures provide

a comprehensive overview of the physical characteristics of wall shearing stress in the analyzed flow system. The results contribute to a better understanding of the mechanical forces exerted on the system's wall and their dependence on various flow parameters.

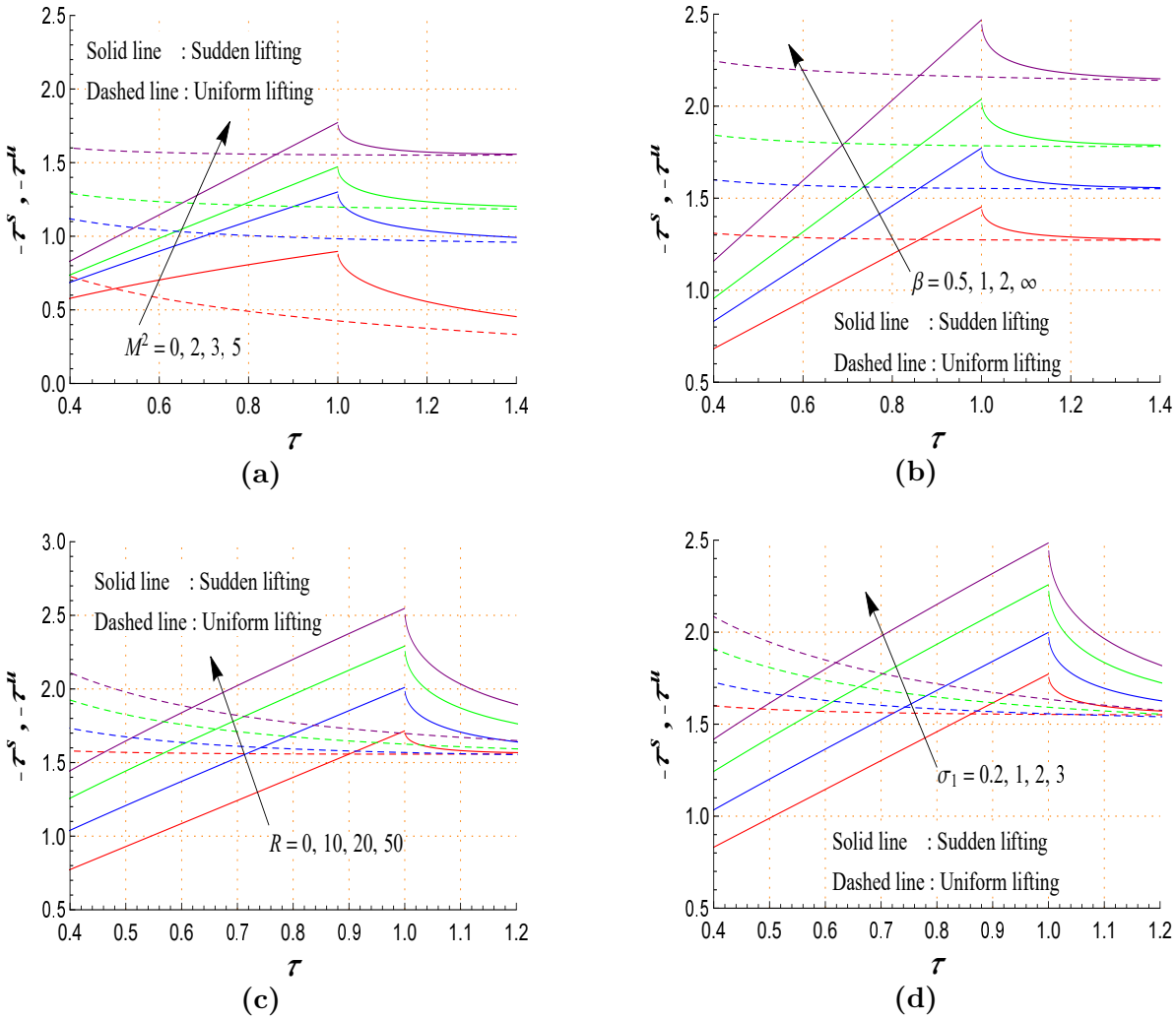

Fig.8: Dispersion of shearing stresses due to working factors

5 Heat transfer rate and dust-phase temperature

Table 3 is included to analyze the behaviour of the rate of heat transfer $-\theta'(0,\tau)$ and the dust phase temperature $\theta_p(0,\tau)$ at the plate against the parametric effects of (Ra, R, γ, α_0, Pr, τ). By examining these data, distinct heat transfer rate patterns and dust-phase temperature patterns can be observed in response to the different factors. From Table 3, it is evident that as the values of (Ra, R, Pr) augment, both $-\theta'(0,\tau)$ and $\theta_p(0,\tau)$ abate, while opposite trend holding for rising values of γ, α_0, and τ. These findings indicate an inverse relationship between the heat transfer rate and the factors (Ra, R, Pr). Growth in the values of Ra results in lessening the thermal zone's width, which reduces the efficiency of convective heat transmission and heat transfer. Because of this, the heat transfer rate goes down. The heat transfer rate and the dust-phase temperature are discovered to be larger when there is no thermal emission occurring, but they reduce with amounting of thermal emission within the flow system. A higher Prandtl number indicates slower thermal diffusion compared to momentum diffusion. This condition results in decreased convective heat transmission and heat transfer, causing a lessening in the heat transfer rate as the Prandtl grows larger. Additionally,

increasing the Newtonian heating parameter α_0 enhances the fluid temperature, thereby enhancing convective heat transmission. Consequently, the heat transmission across the plate upsurges. Moreover, as time progresses, more fluids and dust particles mix, providing more heat available for convection, further increasing the heat transfer rate. In summary, Table 3 provides valuable insights into the heat transfer rate and dust phase temperature behaviour at the thermal plate under different parametric effects. These findings contribute to a better understanding of the factors influencing heat transfer dynamics in the analyzed flow system.

Table 3. Rate of heat transfer $-\theta'(0,\tau)$ and dust-phase temperature $\theta_p(0,\tau)$

Ra	R	γ	α_0	Pr	τ	$-\theta'(0,\tau)$	$\theta_p(0,\tau)$
0	2	3	0.1	7.1	0.5	0.103481	0.02044660
2						0.103280	0.01961740
5						0.103016	0.01849450
2	*0*					0.102927	0.01744710
	2					0.102845	0.01694750
	5					0.102734	0.01627220
		0.5				0.102518	0.00383672
		1				0.102700	0.00750039
		3				0.102845	0.01694750
			0.1			0.102845	0.01694750
			0.2			0.211642	0.03453450
			0.5			0.578105	0.09146680
				0.71		0.106044	0.03817060
				2		0.104659	0.02840170
				7.1		0.102845	0.01694750
					0.1	0.101301	0.00231685
					0.2	0.101831	0.00585095
					0.5	0.102845	0.01694750

6 Statistical paradigm

In this section, we extend the scope of our analysis to assess the associations of different parameter values for the problem under investigation. We employ the correlation coefficient to gain insights into the relationship between physical constraints, shearing stresses, and heat transfer rate. The numerical values for shearing stresses (τ^s, τ^u) and the rate of heat transfer $\theta'(0,\tau)$ are presented in Tables 4 and 5, respectively, along with several relevant parameters of interest.

6.1 Correlation coefficient (CC)

The term *correlation* is commonly used to describe a connection or relationship in everyday life. In the realm of finance and investment, correlation statistics are also employed. However, statistical correlation refers explicitly to the relationship between two quantitative variables. This relationship is assumed to be linear, where one variable changes by a fixed amount for each unit change in the other variable. The strength of this association is quantified by a correlation coefficient, symbolized as r. Pearson's correlation coefficient is the most widely known, although other types also exist. Typically, Pearson's correlation coefficient (r) is used, which ranges from -1 to 1. An error occurred during the correlation calculation if the result exceeded 1 or was less than -1. The correlation coefficient indicates direct and inverse correlations between the two variables and provides insight into their relationship.

The estimation of the correlation coefficient (r) is done using the following formula [44]:

$$r = \frac{\tilde{n}(\sum \tilde{x}\tilde{y}) - (\sum \tilde{x})(\sum \tilde{y})}{\sqrt{\tilde{n}\sum \tilde{x}^2 - (\sum \tilde{x})^2}\sqrt{\tilde{n}\sum \tilde{y}^2 - (\sum \tilde{y})^2}}, \tag{33}$$

where $(\tilde{x}, \tilde{y})$ denotes the bivariate sample of n observations.

The correlation coefficient can be interpreted in several ways:

- When $r = 1$, it indicates a perfect positive linear relationship between the two variables.
- If $r = -1$, it signifies a perfect negative linear relationship between the two variables.
- A strong positive correlation is observed when $0.7 \leq r \leq 1$.
- A strong negative correlation is indicated when $-1 \leq r \leq -0.7$.
- When $r = 0$, it suggests that there is no linear relationship between the variables.

These interpretations provide insights into the strength and direction of the relationship between the variables based on the value of the correlation coefficient.

6.2 Probable error (PE)

The probable error plays a crucial role in estimating the significance and precision of correlation coefficients. It helps assess the reliability of these coefficients by establishing upper and lower bounds within which the correlation coefficient is expected to lie. We can establish these bounds by adding or subtracting the probable error from the correlation coefficient. The probable error of the correlation coefficient can be calculated using the following formula [44]:

$$\mathrm{PE}(r) = 0.6745\left(\frac{1 - r^2}{\sqrt{\tilde{n}}}\right). \tag{34}$$

When the correlation coefficient (r) is smaller than the probable error PE(r), it indicates a lack of correlation between the variables. In such cases, the correlation coefficient is considered insignificant. Conversely, if the value of r is six times greater than the probable error PE(r), it suggests a significant correlation [44].

In order to assess the precision of the correlation coefficient value, PE(r) is calculated. Tables 4 and 5 lists the probable error values for shearing stresses and rate of heat transfer on the plate, respectively. Table 4 contains the values of $\frac{|r|}{PE(r)}$ for the shearing stresses (τ^s, τ^u). It demonstrates that the parameters (M^2, β, R, σ_1) associated with the shearing stresses (τ^s, τ^u) meet the condition $\frac{|r|}{PE(r)} > 6$, indicating their statistical significance for both sudden lifting (SL) and uniform lifting (UL) of the thermal plate. However, for the time parameter τ in the case of uniform lifting (UL), $1 < \frac{|r|}{PE(r)} < 6$, implying a weak association with the shearing stresses. The particle relaxation time parameter σ_1 exhibits a relatively stronger correlation magnitude. Table 5 displays the assessed values of $\frac{|r|}{PE(r)}$ for the rate of heat transfer $\theta'(0, \tau)$. The condition $\frac{|r|}{PE(r)} > 6$ is satisfied for the parameters (Ra, R, γ, α_0, Pr, τ), indicating their significant association with the rate of heat transfer at the plate. The particle concentration parameter R substantially connects with the heat transfer rate. The degree of correlation is comparatively stronger for the particle relaxation time parameter σ_1.

Table 4.Values of r, $PE(r)$, and $\frac{|r|}{PE(r)}$ for the shearing stresses (τ^s, τ^u)

	r		$PE(r)$		$\frac{\|r\|}{PE(r)}$	
Parameter	SL	UL	SL	UL	SL	UL
M^2	-0.998810	-0.996966	0.00080204	0.00204334	1245.34	487.910
β	-0.862604	-0.864182	0.08630700	0.08538800	9.99461	10.1207
R	-0.995293	-0.998620	0.00316722	0.00093009	314.248	1073.68
σ_1	-0.993000	-0.999637	0.00470488	0.00024464	211.058	4086.22
τ	-0.984591	$+0.758985$	0.01031320	0.14297400	95.4693	5.30855

Table 5.Values of r, $PE(r)$, and $\frac{|r|}{PE(r)}$ for the rate of heat transfer $\theta'(0,\tau)$

Parameter	r	$PE(r)$	$\frac{\|r\|}{PE(r)}$
Ra	-0.997257	0.00184792	539.663
R	-0.998501	0.00101025	988.366
γ	$+0.912345$	0.05653240	16.1384
α_0	$+0.999418$	0.00039217	2548.43
Pr	-0.963866	0.02393210	40.2750
τ	$+0.990059$	0.00667206	148.389

6.3 Conclusions

In this manuscript, a theoretical investigation of the magnetically influenced flow of a dusty fluid due to the ramped pace of a thermal plate is conducted. The flow dynamism is observed in the existence of magnetohydrodynamics, thermal emission, heat generation, and Newtonian heating condition. Exact solutions for the resultant system equations are computed opting the Laplace transform (LT). The influence of several distinct factors on curves depicting velocity, temperature, and shearing stress may be shown graphically. In order to illustrate the most critical features, such as heat transmission, tabular representations are used. The major findings are:

- The flow velocity deteriorates for both the fluid-phase and dust-phase declines for higher estimates of magnetic and particle relaxation time parameters, while it enhances with time.
- The velocity distribution is lower for sudden lifting (SL) and higher for uniform lifting (UL).
- The thermal distribution declines as radiation parameter enlarges, while it shows a reverse trend with increasing Newtonian heating parameter.
- The thermal relaxation time parameter enhances the temperature for both the fluid-phase and dust-phase.
- The temperature of the fluid-phase is superior than that of the dust-phase.
- A growth in the values of magnetic, Casson and particle concentration parameters results in a growth in the absolute value of the shearing stress on the thermal plate for both SL and UL situations.
- The absolute value of the shearing stress is seemed to reduce with time for UL.
- The rate of heat transfer rate at the plate is abated due to higher radiation parameter, while it hikes with higher Newtonian heating parameter.

- There is a noteworthy association between the particle relaxation time parameter and shearing stresses.

The ongoing investigation significantly impacts the application of technology and science in today's world. The research findings indicate that fluid-dust suspension, also known as dusty fluid, has various practical applications. For instance, in agriculture, dusty fluid can be combined with water to create a suspension that can be sprayed over crops, improving the effectiveness of pesticide application. It can also be employed in air filtration systems to enhance indoor air quality by capturing airborne particles. Moreover, the results of this investigation have broad implications for climate dynamics, chemical industries, pharmaceuticals, food processing, remediation processes, combustion and energy generation, coal-fired power plants, sediment transport, and related fields. The findings hold particular importance in these disciplines, providing valuable insights and potential advancements.

Conflict of Interest

Authors do not have any conflict of interest.

Data Availability Statement

Data will be available on request.

Funding

No funding available for this research work.

Nomenclature

List of symbols	Description
B_0	Strength of magnetic field (T)
c_p	Fluid-phase specific heat at constant pressure (J $kg^{-1}K^{-1}$)
c_s	Dust-phase specific heat at constant pressure (J $kg^{-1}K^{-1}$)
e_{ij}	Shear strain (Pa)
e_{λ_0}	Plancks function
g	Acceleration due to gravity (m s^{-2})
Gr	Thermal Grashof number
H	Heaviside unit step function
h_T	Convective heat transfer coefficient (W $m^{-2}K^{-1}$)
k	Thermal conductivity (W $m^{-1}K^{-1}$)
k_0	Stokes' resistance (kg m s^{-2})
K_{λ_0}	Absorption coefficient (m^{-1})
m	Average mass of a dust particle (kg)
M^2	Magnetic parameter
N	Number density of dust particles
p_y	Yield stress (N m^{-2})
Pr	Prandtl number
q_r	Radiative heat flux (kg s^{-3})
r	Correlation coefficient
R	Particle concentration parameter
Ra	Radiation parameter
t	Time (s)
t_0	Characteristic time (s)
T	Fluid phase temperature (K)
T_p	Dust phase temperature (K)
T_∞	Constant ambient temperature (K)
u_0	Reference velocity (m s^{-1})
u	Fluid velocity (m s^{-1})
u_1	Dimensionless fluid velocity
(x, y)	Cartesian coordinates (m)

Greek symbols

α_0	Newtonian heating parameter
β	Casson parameter
β^*	Volumetric thermal expansion coefficient (K^{-1})
γ_T	Thermal relaxation time (s)
η	Dimensionless variable
θ	Dimensionless fluid-phase temperature
θ_p	Dimensionless dust-phase temperature
λ	Thermal radiation wavelength (m)
μ_b	Plastic dynamic viscosity (kg $m^{-1}s^{-1}$)
ξ	Laplace transform parameter
ρ	Fluid-phase density (kg m^{-3})
ρ_p	Dust-phase density (kg m^{-3})
σ	Electrical conductivity ($\Omega^{-1}m^{-1}$)
σ_1	Particle relaxation time parameter
τ	Dimensionless time
τ_{ij}	Stress tensor (N m^{-2})

Abbreviation

CC	Correlation coefficient
DF	Dusty fluid
LT	Laplace transform
MHD	Magnetodydrodynamics
PE	Probable error
SL	Sudden lifting
UL	Uniform lifting

Appendix A

The following constant expressions are utilized in the results.

$$
\begin{aligned}
a &= Pr + \frac{2}{3}\frac{R}{\gamma},\ b = \frac{Ra}{a},\ a_0 = -\frac{\alpha_0}{\sqrt{a}},\ \beta_0 = 1 + \frac{1}{\beta}, \\
c &= \frac{1}{\beta_0}(1 + \frac{R}{\lambda_2}),\ c_0 = \frac{a_0}{a-c},\ \lambda_1 = \frac{M^2}{1 + R/\lambda_2},\ \lambda_2 = \frac{1}{\sigma_1},\ \lambda_3 = \frac{c_0 Gr}{\beta_0}, \\
\beta_1 &= \frac{c\lambda_1 - ab}{a-c},\ \beta_2 = a_0^2 - b, \\
\psi_1(x, e_0, e_1, y) &= L^{-1}\left[\frac{e^{-\sqrt{\xi+e_1}\,x}}{\xi(e_0 + \sqrt{\xi + e_1})}\right] \\
&= -\frac{e_0}{e_0^2 - e_1} e^{e_0 x + (e_0^2 - e_1)y} \mathrm{efrc}(\frac{x}{2\sqrt{y}} + e_0\sqrt{y}) \\
&+ \frac{1}{2(e_0^2 - e_1)}[(e_0 + \sqrt{e_1})e^{x\sqrt{e_1}}\,\mathrm{efrc}(\frac{x}{2\sqrt{y}} + \sqrt{e_1 y}) \\
&+ (e_0 - \sqrt{e_1})e^{-x\sqrt{e_1}}\,\mathrm{efrc}(\frac{x}{2\sqrt{y}} - \sqrt{e_1 y})], \\
\psi_2(x, e_0, y) &= L^{-1}\left[\frac{e^{-\sqrt{\xi+e_0}\,x}}{\xi^2}\right] \\
&= \frac{1}{2}[(y + \frac{x}{2\sqrt{e_0}})e^{x\sqrt{e_0}}\mathrm{erfc}(\frac{x}{2\sqrt{y}} + \sqrt{e_0 y})
\end{aligned}
$$

$$
\begin{aligned}
&+ \quad (y - \frac{x}{2\sqrt{e_0}})e^{-x\sqrt{e_0}}\mathrm{erfc}(\frac{x}{2\sqrt{y}} - \sqrt{e_0 y})], \\
\psi_3(x, e_0, e_1, e_2, y) &= L^{-1}\left[\frac{e^{-\sqrt{(\xi+e_1)}\,x}}{\xi(\xi - e_2)(e_0 + \sqrt{\xi + e_1})}\right] \\
&= -\frac{e_0}{(e_0^2 - e_1)(e_0^2 - e_1 - e_2)}e^{e_0 x + (e_0^2 - e_1)y}\mathrm{efrc}(\frac{x}{2\sqrt{y}} + e_0\sqrt{y}) \\
&+ \quad \frac{e^{-e_2 y}}{2e_2(e_0^2 - e_1 - e_2)}[(e_0 + \sqrt{e_1 + e_2})e^{x\sqrt{e_1+e_2}}\,\mathrm{efrc}(\frac{x}{2\sqrt{y}} + \sqrt{(e_1 + e_2)y}) \\
&+ \quad (e_0 - \sqrt{e_1 - e_2})e^{-x\sqrt{e_1+e_2}}\,\mathrm{efrc}(\frac{x}{2\sqrt{y}} - \sqrt{(e_1 + e_2)y})] \\
&- \quad \frac{1}{2e_2(e_0^2 - e_1)}[(e_0 + \sqrt{e_1})e^{x\sqrt{e_1}}\,\mathrm{efrc}(\frac{x}{2\sqrt{y}} + \sqrt{e_1 y}) \\
&+ \quad (e_0 - \sqrt{e_1})e^{-x\sqrt{e_1}}\,\mathrm{efrc}(\frac{x}{2\sqrt{y}} - \sqrt{e_1 y})], \\
\psi_4(x, e_0, e_1, e_2, e_3, e_4, \tau) &= L^{-1}\left[\frac{e^{-\sqrt{\xi+e_1}\,x}}{\xi(\xi - e_3)(e_0 + \sqrt{\xi + e_2})}\right] \\
&= [\frac{1}{e_3 - e_4}(\frac{e_2}{e_3} + 1)\psi_5(x, e_1, e_2, e_3, y) \\
&+ \quad \frac{1}{e_4 - e_3}(\frac{e_2}{e_4} + 1)\psi_5(x, e_1, e_4, e_2, y) + \frac{1}{e_3 e_4}\psi_5(x, e_1, 0, e_2, y)] \\
&- \quad e_0[\frac{1}{e_3(e_3 - e_4)}\psi_6(x, e_1, e_3, y) + \frac{1}{e_4(e_4 - e_3)}\psi_6(x, e_1, e_4, y) \\
&+ \quad \frac{1}{e_3 e_4}\psi_6(x, e_1, 0, y)], \\
\psi_5(x, e_0, e_1, e_2, y) &= L^{-1}\left[\frac{e^{-\sqrt{\xi+e_0}\,x}}{(\xi - e_2)\sqrt{\xi + e_1}}\right] \\
&= \frac{\sqrt{e_0 + e_2}}{2(e_3 + e_1)}e^{e_2 y}[e^{-x\sqrt{e_0+e_2}}\mathrm{erfc}\{\frac{x}{2\sqrt{y}} - \sqrt{(e_0 + e_2)y}\} \\
&- \quad e^{-x\sqrt{e_0+e_2}}\mathrm{erfc}\{\frac{x}{2\sqrt{y}} + \sqrt{(e_0 + e_2)y}\}] \\
&+ \quad \frac{i\sqrt{e_1 - e_0}}{2(e_2 + e_1)}e^{-e_1 y}[e^{ix\sqrt{e_1-e_0}}\mathrm{erfc}\{\frac{x}{2\sqrt{y}} + i\sqrt{(e_1 - e_0)y}\} \\
&- \quad e^{-ix\sqrt{e_1-e_0}}\mathrm{erfc}\{\frac{x}{2\sqrt{y}} - i\sqrt{(e_1 - e_0)y}\}], \\
\psi_6(x, e_0, e_1, y) &= L^{-1}\left[\frac{e^{-\sqrt{\xi+e_0}\,x}}{\xi - e_1}\right] \\
&= \frac{1}{2}e^{e_1 y}[e^{x\sqrt{e_0+e_1}}\mathrm{erfc}\{\frac{x}{2\sqrt{y}} + \sqrt{(e_0 + e_1)y}\} \\
&+ \quad e^{-x\sqrt{e_0+e_1}}\mathrm{erfc}\{\frac{x}{2\sqrt{y}} - \sqrt{(e_0 + e_1)y}\}], \\
\psi_7(x, e_0, e_1, y) &= L^{-1}\left[\frac{e^{-\sqrt{\xi+e_0}\,x}}{\xi^2(\xi - e_1)}\right] \\
&= \frac{1}{2e_1^2}e^{e_1 \tau}[e^{x\sqrt{e_0+e_1}}\mathrm{erfc}\{\frac{x}{2\sqrt{y}} + \sqrt{(e_0 + e_1)y}\}
\end{aligned}
$$

$$
\begin{aligned}
&+ \quad e^{-x\sqrt{e_0+e_1}}\operatorname{erfc}\{\frac{x}{2\sqrt{y}} - \sqrt{(e_0+e_1)y}\}] \\
&- \quad \frac{1}{2e_1}[(y + \frac{1}{e_1} + \frac{x}{2\sqrt{e_0}})e^{x\sqrt{e_0}}\operatorname{erfc}(\frac{x}{2\sqrt{y}} + \sqrt{e_0 y}) \\
&+ \quad (y + \frac{1}{e_1} - \frac{x}{2\sqrt{e_0}})e^{-x\sqrt{e_0}}\operatorname{erfc}(\frac{x}{2\sqrt{y}} - \sqrt{e_0 y})], \\
\psi_8(x, e_0, y) &= L^{-1}\left[\frac{e^{-\sqrt{\xi+e_0}\,x}}{\xi}\right] \\
&= \frac{1}{2}[e^{x\sqrt{e_0}}\operatorname{erfc}(\frac{x}{2\sqrt{y}} + \sqrt{e_0 y}) + e^{-x\sqrt{e_0}}\operatorname{erfc}(\frac{x}{2\sqrt{y}} - \sqrt{e_0 y})], \\
\psi_1'(0, e_0, e_1, y) &= \frac{e_0^2}{e_0^2 - e_1}e^{(e_0^2-e_1)y}[e_0\operatorname{efrc}(e_0\sqrt{y}) - \frac{1}{\sqrt{\pi y}}e^{-e_0^2 y}] \\
&+ \quad \frac{1}{e_0^2 - e_1}[e_0\sqrt{e_1}\operatorname{efr}(\sqrt{e_1 y}) + \frac{e_0}{\sqrt{\pi y}}e^{-e_1 y} - e_1], \\
\psi_2'(0, e_0, y) &= -[(y\sqrt{e_0} + \frac{1}{2\sqrt{e_0}})\operatorname{erf}(\sqrt{e_0 y}) + \sqrt{\frac{y}{\pi}}e^{-e_0 y}], \\
\psi_3'(0, e_0, e_1, e_2, y) &= -\frac{e_0^2 e^{(e_0^2-e_1)y}}{(e_0^2 - e_1)(e_0^2 - e_1 - e_2)}[e_0\operatorname{efrc}(e_0\sqrt{y}) - \frac{1}{\sqrt{\pi y}}e^{-e_0^2 y}] \\
&- \quad \frac{e^{e_2 y}}{e_2(e_0^2 - e_1 - e_2)}[e_0\sqrt{e_1 + e_2}\operatorname{efr}(\sqrt{(e_1+e_2)y}) \\
&+ \quad \frac{e_0}{\sqrt{\pi y}}e^{-(e_1+e_2)y} - (e_1 + e_2)] + \frac{1}{e_2(e_0^2 - e_1)}[e_0\sqrt{e_1}\operatorname{efr}(\sqrt{e_1 y}) \\
&+ \quad \frac{e_0}{\sqrt{\pi y}}e^{-e_1 y} - e_1], \\
\psi_5'(0, e_0, e_1, e_2, y) &= -[(e_0 + e_3)e^{e_3 y} - (e_0 - e_2)e^{-e_2 y}], \\
\psi_6'(0, e_0, e_1, y) &= -e^{e_1 y}[\sqrt{e_1 + e_2}\operatorname{efr}(\sqrt{(e_1+e_2)y}) + \frac{1}{\sqrt{\pi y}}e^{-(e_1+e_2)y}], \\
\psi_8'(0, e_0, y) &= -[\sqrt{e_0}\operatorname{efr}(\sqrt{e_0 y}) + \frac{1}{\sqrt{\pi y}}e^{-e_0 y}]
\end{aligned}
$$

References

[1] R.A. Hamid, R. Nazar, I. Pop, Numerical solutions for unsteady boundary layer flow of a dusty fluid past a permeable stretching/shrinking surface with particulate viscous effect, Int. J. Numer. Method H. 28 (2018) 13741391

[2] B. Mahanthesh, N.S. Shashikumar, B.J. Gireesha, I.L. Animasaun, Effectiveness of hall current and exponential heat source on unsteady heat transport of dusty TiO2-EO nanoliquid with non-linear radiative heat, J. Comput. Des. Eng. 6 (2019) 551-561.

[3] C.E. Nanjundappa, A. Pavithra, I.S. Shivakuamara, Effect of dusty particles on Darcy-Brinkman gravity-driven ferro-thermal-convection in a ferrofluid saturated porous layer with internal heat source: Influence of boundaries, Int. J. Appl. Comput. Math. 7 (2021) 1-20.

[4] M. Radhika, R.J. Punith Gowda, R. Naveenkumara, B.C. Prasannakumara, Heat transfer in dusty fluid with suspended hybrid nanoparticles over a melting surface, Heat Transf. 50 (3) (2021) 2150-2167.

[5] M. R. Islam, M. Ferdows, J. C. Misra, M. G. Murtaza, Two-dimensional thin layer convective flow and heat transfer of a dusty fluid on a nonlinear stretching sheet, Multiscale Sci. Eng. 4 (2022) 111-118.

[6] D. Dey, B. Chutia, Dusty nanofluid flow with bioconvection past a vertical stretching surface, J. King Saud. Univ. Eng. Sci. 34 (2022) 375-380.

[7] N. Casson, A flow equation for the pigment oil suspensions of the printing ink type, Rheology of Disperse systems, Pergamon Press: New York, NY, USA, 1959.

[8] B. Mahanthesh, O. D. Makinde, B. J. Gireesha, K. L. Krupalakshmi, I. L. Animasaun, Two-phase flow of dusty Casson fluid with Cattaneo-Christov heat flux and heat source past a cone, wedge and plate, Defect Diffus. Forum. 387 (2018) 625-639.

[9] B. Mahanthesh, I. Animasaun, M. Rahimi-Gorji, I.M. Alarifi, Quadratic convective transport of dusty Casson and dusty Carreau fluids past a stretched surface with nonlinear thermal radiation, convective condition and non-uniform heat source/sink, Phys. A.: Stat. Mech. Appl .535 (2019) 122471.

[10] F.M. Hady, A. Mahdy, R.A. Mohamed, S.E. Ahmed, O.A. Abo-zaid, Unsteady natural convection flow of a dusty non-Newtonian Casson fluid along a vertical wavy plate: numerical approach, J. Braz. Soc. Mech. Sci. Eng. 41 (11) (2019) 120.

[11] D. Khan, P. Kumam, W. Kumam, P. Suttiarporn, A. Rehman, Relative magnetic field and slipping effect on Casson dusty fluid of two phase fluctuating flow over inclined parallel plate, S. Afr. J. Chem. Eng. 44 (2023) 135-146.

[12] S. Das, A. Ali, R.N. Jana, Impact of hall currents with buoyancy forces on hydromagnetic reactive Casson fluid flow past a slippery plate in a rotating porous medium, Special Topics Rev. Porous Media 11(4) (2022) 313-340

[13] S. Das, A.S. Banu, R.N. Jana, Delineating impacts of non-uniform wall temperature and concentration on time-dependent radiation-convection of Casson fluid under magnetic field and chemical reaction, World J. Eng. 18 (5)(2021) 780-795.

[14] G. Ali, F. Ali, A. Khan, A. H. Ganie, I. Khan, A generalized magnetohydrodynamic two-phase free convection flow of dusty Casson fluid between parallel plates, Case Stud. Therm. Eng. 29 (2022) 101657.

[15] A. C. Cogley, W. C. Vincenti, S. E. Gilles, Differential approximation for radiation transfer in a non-grey gas near equilibrium, AIAA J. 6(3) (1968) 551-555.

[16] N. Pandya, R.K. Yadav, A.K. Shukla, Combined effects of Soret-Dufour, radiation and chemical reaction on unsteady MHD flow of dusty fluid over inclined porous plate embedded in porous medium, Int. J. Adv. Appl. Math. Mech. 5 (2017) 49-58.

[17] S. Ghadikolaei, K. Hosseinzadeh, D. Ganji, Numerical study on magnetohydrodynic CNTs-water nanofluids as a micropolar dusty fluid influenced by non-linear thermal radiation and Joule heating effect, Powder Technol. 340 (2018)389-399.

[18] B. Mahanthesh, J. Mackolil, M. Radhika, W. Al-Kouz, Significance of quadratic thermal radiation and quadratic convection on boundary layer two-phase flow of a dusty nano liquid past a vertical plate, Int. Commun. Heat Mass Transf. 120 (2021) 105029.

[19] M.V. Krishna, Hall and ion slip effects on radiative MHD rotating flow of Jeffreys fluid past an infinite vertical flat porous surface with ramped wall velocity and temperature, Int. Commun. Heat Mass Transf. 126, 105399 (2021)

[20] M. G. Reddy, M. S. Rani, K. G. Kumar, B. Prasannakumar, H. Lokesh, Hybrid dusty fluid flow through a Cattaneo-Christov heat flux model, Phys. A: Stat. Mech. 551 (2020) 123975.

[21] W. Abbas, K.S. Mekheimer, M.M. Ghazy, A. Moawad, Thermal radiation effects on oscillatory squeeze flow with a particle-fluid suspension, Heat Transf. 50 (2020) 2129-2149.

[22] S. Das, N. Mahato, A. Ali, R.N. Jana, Dynamics pattern of a radioactive rGO-magnetite-water flowed by a vibrated Riga plate sensor with ramped temperature and concentration, Chem. Eng. J. Adv. 15 (2023) 100517.

[23] S. Ahmad, S. Nadeem, Application of CNT-based micropolar hybrid nanofluid flow in the presence of Newtonian heating, Appl. Nanosci. 10 (12) (2020) 52655277.

[24] S. Das, C. Mandal, R.N. Jana, Unsteady mixed convection flow past a vertical plate with newtonian heating, Int. J. Energy Tech. 6 (2014) 1-9.

[25] M. Das, R. Mahato, R. Nandkeolyar, Newtonian heating effect on unsteady hydromagnetic Casson fluid flow past a flat plate with heat and mass transfer, Alex. Eng. J. 54(4) (2015) 871-879.

[26] S.M. Upadhya, C.S.K. Raju, S. Saleem, A.A. Alderremy, Mahesha, Modified Fourier heat flux on MHD flow over stretched cylinder filled with dust, graphene and silver nanoparticles, Results Phys. 9 (2018) 1377-1385.

[27] A. Khan, D. Khan, I. Khan, F. Ali, F.U. Karim, M. Imran, MHD flow of sodium alginate-based Casson type nanofluid passing through porous medium with Newtonian heating, Sci. Rep. 8(1) (2018) 1-12.

[28] A. Ali, S. Das, R. N. Jana, MHD gyrating stream of non-Newtonian modified hybrid nanofluid past a vertical plate with ramped motion, Newtonian heating and Hall currents, Z. Angew. Math. Mech. (2023), https://doi.org/10.1002/zamm.202200080

[29] M. Kamran, B. Wiwatanapataphee, Chemical reaction and Newtonian heating effects on steady convection flow of a micropolar fluid with second order slip at the boundary, Eur. J. Mech. B Fluid 71 (2018) 138-150.

[30] F. Hady, A. Mahdy, R. Mohamed, O. A. A. Zaid, Modeling non-Darcy natural convection flow of a micropolar dusty fluid with convective boundary condition, Int. J. Aerosp. Eng. 14 (2020) 53-59.

[31] D. Qaiser, Z. Zheng, M. R. Khan, Numerical assessment of mixed convection flow of Walters-B nanofluid over a stretching surface with Newtonian heating and mass transfer, Therm. Sci. Eng. Prog. 22 (2021), 100801.

[32] D. Khan, P. Kumam, A. ur Rahman, G. Ali, K. Sitthithakerngkiet, W. Watthayu, A. M. Galal, The outcome of Newtonian heating on Couette flow of viscoelastic dusty fluid along with the heat transfer in a rotating frame: second law analysis, Heliyon 8 (2022) e10538.

[33] R. Nandkeolyar, G. S. Seth, O. D. Makinde, P. Sibanda, Md. S. Ansari, Unsteady hydromagnetic natural convection flow of a dusty fluid past an impulsively moving vertical plate with ramped temperature in the presence of thermal radiation, J. Appl. Mech. 80(6) (2013) 061003.

[34] Hazarika, G.C., Konch, J. Effects of variable viscosity and thermal conductivity on magneto-hydrodynamic free convection dusty fluid along a vertical porous plate with heat generation. Turk. J. Phys. 40 (1) (2016) 5268.

[35] M. Jalil, S. Asghar, S. Yasmeen, An exact solution of MHD boundary layer flow of dusty fluid over a stretching surface, Math. Probl. Eng. 2017(2017) 15.

[36] M. Turkyilmazoglu, Magnetohydrodynamic two-phase dusty fluid flow and heat model over deforming isothermal surfaces, Phys. Fluids. 29 (2017), 013302.

[37] B. Gireesha, B. Mahanthesh, G. Thammanna, P. Sampathkumar, Hall effects on dusty nanofluid two-phase transient flow past a stretching sheet using KVL model, J. Mol. Liq. 256 (2018)139-147.

[38] O. A. Abo-zaid, R. A. Mohamed, F. M. Hady, A. Mahdy, MHD Powell-Eyring dusty nanofluid flow due to stretching surface with heat flux boundary condition, J. Egypt. Math. Soc. 29 (2021) 114.

[39] R. A. Hamid, R. Nazar, K. Naganthran, I. Pop, Dusty ferrofluid transport phenomena towards a non-isothermal moving surface with viscous dissipation, Chin. J. Phys. 75 (2022) 139-151.

[40] S.R. Mishra, T.-C. Sun, B.C. Rout, M. I. Khan, M. K. Alaoui, S. U. Khan, Control of dusty nanofluid due to the interaction on dust particles in a conducting medium: numerical investigation, Alex. Eng. J. 61 (2022) 3341-3349.

[41] N. Sandeep, C. Sulochana, B.R. Kumar, Unsteady MHD radiative flow and heat transfer of a dusty nanofluid over an exponentially stretching surface, Int. J. Eng. Sci. Technol. 19 (2016) 227240.

[42] B. K. Jha, Y. J. Danjuma, Transient generalized Taylor-Couette flow of a dusty fluid: A semi-analytical approach, Partial Differ. Equ. Appl. Math. 5 (2022) 100400.

[43] W. Abbas, O. Khaled, S. Beshir, M. Abdeen, M. Elshabrawy, Analysis of chemical, ion slip, and thermal radiation effects on an unsteady magnetohydrodynamic dusty fluid flow with heat and mass transfer through a porous media between parallel plates, Bull. Natl. Res. Cent. 47 (2023) 49.

[44] S.Das, S.Das, EDL aspects in swirling ionic tribological fluid flow in a squeezed/split channel underlie a high-power magnetic field, Forces Mech. 11 (2023) 100196.